

XSGRB I - The X-shooter GRB afterglow sample [★]

J. Selsing¹ and XSGRB collaboration

Dark Cosmology Centre, Niels Bohr Institute, University of Copenhagen, Juliane Maries Vej 30, 2100 København Ø, Denmark

Received/ accepted

ABSTRACT

In this work we present the spectra of all γ -ray bursts (GRBs) afterglows that have been observed at the VLT/X-shooter up to 31.03.2017. This totals 137 spectroscopic observations of 118 individual bursts, of which redshifts have been secured for 91 % covering a redshift range from 0.059 to ~ 8.5 . Some of these observations are late-time observations of the underlying host galaxy. Based on a set of selection criteria that are unbiased with regards to intrinsic properties of the GRBs, the follow-up effort has been guided by the *Swift*-telescope to produce a homogeneous sample of afterglows for 86 spectra. We here provide a public release of all the reduced spectra, including continuum estimates and telluric corrections. We provide an assessment of the degree of completeness with respect to the parent GRB population, in terms of the X-ray properties of the bursts in the sample and find that the sample presented here is consistent with being drawn from the *Swift* sample. For all bursts (39) for which it is possible, we provide a measurement of the hydrogen column density, increasing the total number of published HI column density measurements by ~ 50 per cent. We constrain the fraction of dark bursts to be less than 28 per cent based on the detection of an optical afterglow and tentatively confirm previous results that larger optical darkness is correlated with increased X-ray absorption. This dataset provides a unique possibility to study the ISM across cosmic time.

Key words. Gamma-ray burst: general — galaxies: high-redshift — ISM: molecules — dust, extinction

1. Introduction

Gamma-Ray bursts (GRBs) are interesting as they provide the opportunity to derive new constraints on a very wide range of topics in astrophysics. Examples range from small scale phenomena relating to magnetars, properties of highly relativistic jets, hyper/supernova explosions, the interstellar medium, dust extinction curves, starburst galaxies, chemical and molecular abundances, escape of ionizing radiation, the ionization state of the intergalactic medium, intervening absorption systems to standard candles in cosmology (e.g., [Lyons et al. 2010](#); [Molinari et al. 2006](#); [Hjorth & Bloom 2011](#); [Wijers et al. 1998](#); [Prochaska et al. 2009](#); [Savaglio 2006](#); [Ghirlanda 2007](#)). In that sense GRB research is very multidisciplinary.

The *Swift* satellite ([Gehrels et al. 2009](#)), which was launched in 2004, has made it possible to harvest much of the great potential in using GRBs as probes of galaxies in the intergalactic medium, which was already hinted at by results from earlier missions (e.g., [Ricker & Team 2004](#)). A crucial aspect of the great success of the *Swift* mission has been the extensive ground based follow-up observations of the afterglows and of the host galaxies of the GRBs. This work has involved a large community of researchers both inside and outside the official *Swift* team. This fruitful collaboration has been greatly facilitated by the open data access policy of the *Swift* mission.

In the beginning of the "*Swift* era" most of the follow-up spectroscopy was secured using low-resolution spectrographs (typically $R=\lambda/\Delta\lambda < 1000$, e.g. [Fynbo et al. 2009](#)). Low-resolution spectroscopy is powerful for a number of reasons, first

of all is the ability to secure information for even very faint targets. This allows the measurements of a number of important parameters such as redshifts, spectral slopes, and extinction. For a handful of very bright afterglows high-resolution (typically $R > 20000$) spectra were secured, and for these events much more information about conditions inside the host galaxies were extracted (e.g., [Fiore et al. 2005](#); [Thone et al. 2007](#); [Prochaska et al. 2007](#); [Vreeswijk et al. 2007](#); [Castro-Tirado et al. 2010](#)).

The X-shooter spectrograph ([Vernet et al. 2011](#)) is the first of the 2nd generation instruments at the ESO Very Large Telescope (VLT). It is a high-throughput echelle spectrograph covering the full spectral range from the UV atmospheric cutoff around 300 nm to the near-infrared (near-IR) K-band ending around 2500 nm with three spectral arms (UVB, VIS, NIR). It was designed very much with transient source follow-up in mind as the fading luminosities of such sources makes it urgent to secure as extensive coverage as possible in the shortest possible time. At the same time, the resolution was designed to be in the range 4000–9000 in order to be able to get a large useful spectral range between the many sky-background emission lines in the red and near-IR spectral ranges.

In this paper, we present the results of a dedicated effort over the years 2009 – 2017 to use the X-shooter spectrograph to secure spectroscopic observations of afterglows and host galaxies of GRBs detected by *Swift*. We here make all data resulting from the survey, publicly available in reduced form.

The paper is organized in the following way: In Sect. 2 we describe the sample including the sample selection criteria and the observational strategy. In Sect. 3, we describe the observations and the instrumental setups, and in Sect. 4 we detail the methodological strategies adopted in the data reduction process and auxiliary material. In Sect. 5 we describe the results of the survey, i.e. the efficiency of the follow-up effort and the charac-

[★] Based on observations collected at the European Southern Observatory, Paranal, Chile, Program ID: 098.A-0055, 097.A-0036, 096.A-0079, 095.B-0811(B), 095.A-0045, 094.A-0134, 093.A-0069, 092.A-0124, 0091.C-0934, 090.A-0088, 089.A-0067, 088.A-0051, 087.A-0055, 086.A-0073, 085.A-0009 and 084.A-0260

teristics of the observed bursts. We also here assess the completeness of the finally realized sample. Finally, we offer our conclusions in Sect. 6.

2. Sample selection criteria and observations

2.1. Sample selection criteria

Being of transient nature, it is difficult to impose strong sample selection criteria on GRBs, without hampering the follow-up effort. Many natural follow-up restrictions exist already, being it weather conditions, pointing restrictions of the telescope or poorly localized bursts as reported by the alerting telescope. To maximize the return of the follow-up campaign, we have chosen a few selection criteria that facilitates an unbiased selection of bursts, while at the same time allowing for a high follow-up success rate. The importance of defining unbiased selection criteria has been highlighted previously (Jakobsson et al. 2006; Salvaterra et al. 2012; Hjorth et al. 2012; Vergani et al. 2015; Perley et al. 2016a), when trying to address the intrinsic underlying distribution functions such as the redshift distribution, host metallicity distribution, or afterglow brightness distribution. When investigating a specific distribution function, a high degree of completeness is desired (e.g., Perley et al. 2016b).

In defining the selection criteria, we simultaneously aim to minimize any biases against intrinsic astrophysical conditions while at the same time maximizing the likelihood of successful observations, hence allowing us to obtain a higher degree of completeness. By restricting the selection criteria to conditions local to the Milky Way and therefore independent of intrinsic GRB properties, the aim is that the sample collected represents the underlying distribution of GRBs in a fair way. The selection criteria used here is based on previous, similar studies (Jakobsen et al. 2006; Fynbo et al. 2009; Hjorth et al. 2012). We characterize the sample completeness in Sect. 5.2.

Our selection criteria are:

1. GRB triggered by *Swift*.
2. XRT started observing within 10 minutes after the GRB; an XRT position must be distributed within 12 hr.
3. The target must be visible for at least 60 minutes at least 30 degrees above the horizon, with the Sun below -12 degrees.¹
4. No closeby bright stars.
5. Galactic $A_V \lesssim 0.5$ mag.

Our ability to observe GRB afterglows is strongly dependent on the timing and the precision of the target positions delivered by the triggering facilities. By selecting only bursts that have been triggered on board the *Swift* space telescope (Gehrels et al. 2004), based on the Burst Alert Telescope (BAT) (Barthelmy et al. 2005), we start out with a homogeneously selected sample where burst characteristics are delivered immediately, allowing for an informed follow-up strategy. Despite the complexity of the triggering mechanism on board *Swift* (Band 2006; Coward et al. 2013), attempts at inferring properties of the underlying GRB population based on the detection thresholds and triggering algorithms have been made (Lien et al. 2014; Graff et al. 2016). Restricting the follow-up effort to bursts detected by *Swift*, we

therefore ensure that the limitations of the parent sample is well studied.

Because the localization accuracy of BAT is 1 - 4 arcminutes (Barthelmy et al. 2005), a secure host identification is in general impossible based on BAT alone. We therefore additionally require an X-ray position from the X-ray Telescope (XRT) (Burrows et al. 2005) to be distributed to the GCN network (Barthelmy 2000) within 10 hours and to account for observing constraints on *Swift* that XRT began observations within 10 minutes. The additional timing requirement of the XRT follow-up means that all bursts in our sample have detected X-ray afterglows. Because the XRT completeness is very high (Burrows et al. 2007), this cut should not alter the parent sample significantly.

To ensure a minimum of observability, we require that the GRB is visible from the telescope site at Cerro Paranal, Chile, for at least 1 hour after the trigger with the sun below -12 degrees. This secures time for the spectroscopic observations to be completed. Since the GRB population is isotropically distributed on the sky as seen from Earth and because the GRB properties does not depend on position on the sky (Briggs et al. 1996), this cut does not influence our ability to fairly sample the underlying GRB population. The same arguments applies to the requirement that there are no nearby bright stars. We additionally require that the Galactic extinction is below $A_V \lesssim 0.5$ mag, based on the extinction maps by Schlegel et al. (1998). Because of isotropy, these additional cuts should not influence the optical properties of the bursts themselves, only our ability to successfully secure observations that allows us to investigate the spectroscopic properties of GRBs.

We further discuss the effect of these selection criteria and their implication for the completeness of the sample in Sect. 5.2.

2.2. Follow-up procedure and practicalities

(Will be written by Daniele)

2.3. RRM observations

Under rare circumstances, the use of the rapid response mode (RRM) has been possible. In case of a promptly visible GRB, a robotic trigger was sent to the telescope if at the moment of the GCN notice the GRB is observable and fulfills the following criteria.

1. GRB triggered by *Swift*.
2. X-shooter mounted at the telescope
3. GRB promptly visible
4. Error radius $< 60''$.
5. No limit on declination.
6. No constraint on Moon phase or distance.
7. Elevation in the sky $> 22^\circ$ (both now and 15 min after the trigger).
8. Sun elevation $< -12^\circ$ (both now and 15 min after the trigger).
9. The X-ray position must be available less than 1 hr after the GRB.
10. The flags `KNOWN_SOURCE`, `COSMIC_RAY`, `DEF_NOT_GRB` are set to false (`PROB_NOT_GRB` can be true).

The use of RRM is unique in the sense that it allows for the detailed study of the temporal variability of the GRB afterglow due to effect of the GRB itself on the surrounding medium (e.g., see Dessauges-Zavadsky et al. 2006; Vreeswijk et al. 2007, 2013, for examples)

¹ Note that in the P84 proposal the criteria have been stated a bit differently, the visibility constraint being replaced by a declination + Sun angle constraint. The below criteria are however those defining the sample.

For 8 of the observed GRBs released here, RRM triggered. One of the RRM triggers is outside the statistical sample and two of the RRM trigger are on short GRBs. The fastest response between *Swift* GRB trigger and the beginning of spectroscopic integration is for GRB 160410A, for which the delay was only 8.4 minutes.

3. Observations

The observations obtained for this sample have been secured with the cross-dispersed echelle spectrograph, X-shooter (Vernet et al. 2011), mounted on one of the two Unit Telescopes at ESO/VLT, UT2 (Kueyen) and UT3 (Melipal) during the duration of this follow-up campaign. The observations have been taken during a period of 8 years corresponding to the ESO observing periods P84 through P98 under the following programme IDs: 098.A-0055, 097.A-0036, 096.A-0079, 095.A-0045, 094.A-0134, 093.A-0069, 092.A-0124, 0091.C-0934, 090.A-0088, 089.A-0067, 088.A-0051, 087.A-0055, 086.A-0073, 085.A-0009 and 084.A-0260. We have included a few additional bursts, from the programmes 092.D-0056(A) (PI: Rau), 092.D-0633(E) (PI: Greiner), and 095.B-0811(B) (PI: Levan). The total collection of spectra represents *all* GRBs that have been followed up by X-shooter up to 31.03.2017.

The first GRB followed up is GRB 090313, observed on the 15th of March, 2009, during the commissioning of X-shooter UT3. The bursts observed during the commissioning or science verification (GRB 090313, GRB 090530, GRB 090809, GRB 090926) are not a part of our statistical sample. The first burst observed after science verification and X-shooter was moved to UT2, is GRB 091018, which thereby constitute the first burst entering our statistical sample. For all bursts that fulfill our sample selection criteria, described in Sect. 2.1, spectroscopic follow-up has been attempted with X-shooter. Various conditions can affect our ability to follow up a given burst, and a discussion of these conditions and their consequences for the sample is included in Sect. 5.3.

X-shooter covers the spectral wavelength region from 300 nm to 2480 nm in a single exposure, by separating the light into three separate spectroscopic arms through the use of two dichroics. The ultraviolet blue (UVB) arm covers 300 - 550 nm, the visual (VIS) arm covers 550 - 1020 nm, and the near-infrared (NIR) arm covers 1020 - 2480 nm. For some of the observations, we have applied a K-band blocking filter, cutting the coverage of the NIR arm at 2100 nm. This is done to reduce the amount of scattered background light from the thermal infrared. For the majority of observations, a nod-and-shuffle observing scheme has been employed, with a nodding throw of 5". Each nodding observation have typically been carried out in a standard ABBA pattern. For some cases, conditions during the follow-up, either technical or weather, have necessitated alterations to this scheme as described in App. B. For RRM triggers, a slightly different observing strategy was employed. Starting as rapidly as possible, a simple stare mode sequence was started, with 5 spectroscopic integrations with increasing exposure times.

For the majority of the bursts, we have observed with a slit width of 1'0, 0'9, and 0'9 for the UVB, VIS, and NIR-arm respectively. This sets a lower limit on the delivered resolution of the spectra based on the tabulated values of the delivered resolutions, which is 4350, 7450, and 5300 for the UVB, VIS and NIR-arm respectively². For accurate measurements involv-

ing line profiles, knowledge of the precise instrumental resolution is required. The resolution becomes better than the nominal one, listed above, when the delivered seeing is smaller than the projected width of the slit on the sky. We discuss how we determine the effective instrumental resolution in Sect. 4.6.

Due to a mechanical failure, the atmospheric dispersion corrector (ADC) was disabled from 1st of August 2012. Only GRB 100728B was affected by the failing ADC prior to disablement, resulting in a lower-than-nominal throughput. To avoid chromatic slit losses due to atmospheric dispersion, all subsequent observations have been carried out at parallactic angle. A consequence of this, is that for all observations following 1st of August 2012, the centroid of spectrum changes position across the spatial direction of the slit as a function of wavelength. This effect has been modeled in the extraction procedure, as described in Sect. 4.3.

We provide an overview of all the observations in Table 1 and plot the positions of all the bursts on the celestial sphere in galactic coordinates in Fig. 1. Away from central zone of avoidance due to high galactic extinction cutoff (marked in white), the GRB positions have an apparent isotropic distribution except in the upper left quadrant, which cannot be observed from Paranal.

A subset of the spectra presented here, primarily host observations, have already been published in Krühler et al. (2015). We include independent reductions of them here for completeness.

4. Data processing

In this section we describe how the final data products are produced and subsequently post-processed. All post-processing scripts developed for this dataset are made publicly available at https://github.com/jselsing/XSGRB_reduction_scripts, along with instructions of use.

Before any reductions are initiated, the raw object images are run through the cosmic-ray removal algorithm (van Dokkum 2001) implementation, *Astro-SCRAPPY*³, where a wide clipping radius have been used around detected cosmics to ensure that edge residuals are robustly rejected.

The basis for the reductions is the VLT/X-shooter pipeline, version 2.7.1 or newer (Goldoni et al. 2006; Modigliani et al. 2010). The pipeline is managed with the Reflex interface (Freudling et al. 2013) and is used for subtraction of bias level, flat-fielding, tracing of the echelle orders, wavelength calibrations with the use of arc-line lamps, flux calibration using spectrophotometric standards (Vernet et al. 2009; Hamuy et al. 1994), mirror flexure compensation, initial sky-subtraction and lastly the rectification and merging of the orders. For the initial sky-subtraction, the background has been estimated in regions adjacent to the object trace clear of contaminating sources. Because of the broken ADC, for some objects there is a lot of curvature in the object trace along the dispersion axis of the slit. This means that for some bursts, the initial sky-estimate has been made from a limited number of pixels in the spatial direction. By doing an initial subtracting the sky on the un-rectified image we ensure that bulk of the sky background is not redistributed by the rectification process.

The image is rectified onto an equidistant grid with a dispersion sampling of 0.02 nm/pixel and a 0.16 "/pixel spatial sampling for the UVB and VIS arm and 0.06 nm/pixel with a 0.21 "/pixel in the NIR arm. Because the tabulated resolution is a lower limit, by choosing a sampling of 0.02 nm/pixel, we ensure that the bluest part of neither of the arms have a sampling

² <https://www.eso.org/sci/facilities/paranal/instruments/xshooter/inst.html>

³ <https://github.com/astroscrappy/astroscrappy>

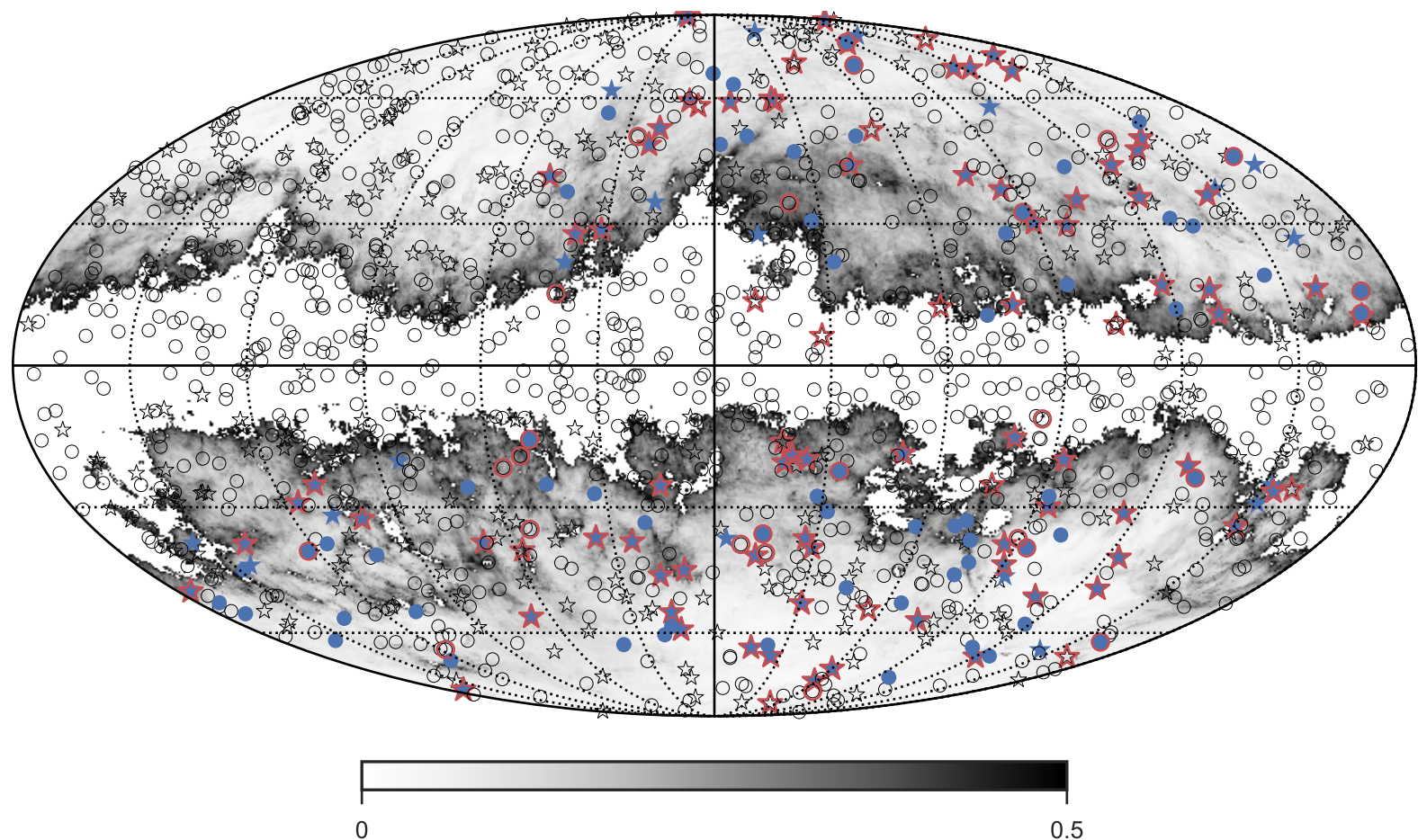


Fig. 1: Mollweide projection in galactic coordinates of the full sky showing the positions on the sky of the bursts presented in this work. The equator is the Galactic plane. The empty circles are the positions of all the *Swift* bursts detected until the end of 2016. In blue is shown the position of the bursts fulfilling the sample criteria specified in Sect. 2.1. The red circles are added around GRBs which have been followed up by X-shooter since the commissioning of the instrument. Blue points with red circles represent GRBs that enter our sample and have X-shooter spectroscopy. The different samples are compared in Sect. 5. The background shows the dust maps presented in [Schlegel et al. \(1998\)](#) where the sample criteria cut with $A_V \lesssim 0.5$ mag is removed. The colorbar below indicates the value of A_V on the plot. The dotted lines indicate intervals of 30° in longitude and latitude.

lower than the Nyquist sampling rate of 2 pixels per resolution FWHM.

4.1. Post-processing

For a typical observation, each of the exposures in the nodding sequence has been reduced as single observation and then subsequently combined to form a single image. Because this strategy is employed, we can reject outliers in the stack and weight by an averaged measure of the inverse variance of the background. When weighting images where the noise in each pixel is dominated by Poisson noise it is important to estimate the background variance in a large enough region, so that any correlation between the signal and the weights are removed. To this end, the weight map is generated by a running median window over the variance map, where the trace has been masked and width of the window is chosen to be wide enough for median variance to be generated on the basis of several hundred pixels. This weighting scheme automatically also optimally combines images of differ-

ent exposure times or images where the background is varying, which is often the case when a burst has been observed close to twilight

For the NIR arm, because the background is very bright and there is a high abundance of broad sky-lines, when there are no contaminating sources in the slit, the sky has been put back on the images and they have been reduced in pairs of two, subtracting the two from each other, keeping the WCS static. This amounts to the regular nodding reduction, only we can reject outliers and weight by the averaged inverse variance map.

By STARE reducing all observations we additionally get a spectrum of the sky, which we can use to calibrate the wavelength solution.

4.2. Correction for offsets in the wavelength calibration

X-shooter, being installed at the VLT Cassegrain focus is prone to flexures during operations. The flexures modify the projection of the slit on the detector with respect to the one obtained in day-

time calibration. This requires a modification of the wavelength solution in order to process correctly the night-time data. Part of this correction is performed by the pipeline using the frames taken during X-shooter Active Flexure Compensation procedure⁴. The remaining offset is corrected by cross-correlating the observed sky spectrum with a synthetic sky spectrum (Noll et al. 2012; Jones et al. 2013) after the continuum, estimated as the mode of all flux values, has been subtracted. To get the correct seeing PSF with which to convolve the synthetic sky an initial refinement of the wavelength solution have been obtained by cross-correlating the observed sky with an unconvolved synthetic sky. This preliminary wavelength calibration is applied to the observed sky. The synthetic spectrum is then convolved with an increasing seeing PSF and the width that minimizes χ^2 with the updated observed sky is chosen to be the effective sky-PSF. Using the synthetic sky with the matched resolution, a final wavelength calibration can then be calculated by cross-correlating the observed sky with the correctly broadened sky spectrum, as a function of a velocity offset. Both a multiplicative and an additive offset to the wavelength calibration has been tested, but in terms of χ^2 , the model with only a multiplicative offset is preferred.

The resulting offsets, which were smaller than 0.01 nm in the UVB and VIS data and smaller than 0.05 nm in the NIR spectra, but changing over short period of time were applied to the corresponding spectra. Using the convolved synthetic sky, the pixels containing the brightest sky lines have been added to the bad pixel map.

4.3. Spectral extraction

To extract the afterglow spectrum from the rectified 2D-image, several techniques have been employed based on the brightness of the afterglow and the complexity of the objects entering the slit. Due to the malfunctioning ADC, see Sect. 3, the spectral trace changes position across the slit in the spatial direction as a function of wavelength. For a large fraction of the bursts observed, using a single aperture for the spectral extraction is inadequate due to the large amount of background that would then enter the slit. To optimally select the extraction regions we therefore need to model the trace position.

To get the shape and the position of the spectral PSF as a function of location on the image, we need to choose a model which can represent how the light falls on the slit. We know from Trujillo et al. (2001) that the Moffat function (Moffat 1969) adequately describes an imaging PSF due to atmospheric turbulence, but because of aberrations in the dispersion elements and the rectification process, the PSF we are trying to model is different from this profile. To allow for flexibility in the model, we have chosen the Voigt function as a model for the spectral PSF and we describe how this is evaluated in App. A. Since additionally, the host galaxy could also have a contribution the image profile, this choice allows for the required freedom if additional flux is in the wings of the profile.

To guide the guess position of the trace on the slit as a function of wavelength, we have used the analytic prescription for the trace position described in Filippenko (1982), where the header keywords of the observations have been queried for the ambient conditions which controls the degree to which the trace changes position in the spatial direction.

Based on the signal-to-noise of the afterglow continuum, the 2D-image has been binned down in the spectral direction to a number of elements that allows for an accurate tracing of the PSF, typically 200 bins for moderate signal-to-noise. For each of the bins, using the analytically guided guess position, the spectral PSF has been fit using the unweighted chi-squared minimization algorithm implemented in `scipy.optimize.curve_fit` (Jones et al. 2001). Since we know that the trace varies slowly as a function of wavelength, we have then fitted a low-order polynomial to the fit parameters as a function of wavelength, which allows us to evaluate the spectral PSF at all wavelengths and this way accurately model the entire spectral PSF.

Equipped with a model for how the light is distributed across the entire dispersion direction, we can employ the optimal extraction algorithm Horne (1986), which weights the extraction aperture by the spectral profile, or alternatively sum all pixels within 1 FWHM of the modeled profile. Where possible, we have used the optimal extraction. In cases where the trace is very weak, even in the binned images, an aperture has been selected manually which covers emission lines, if present, and when nothing is immediately visible, the entire nodding window. The error- and bad pixel maps are in all cases propagated throughout the extraction.

In cases where multiple traces are visible in the slit, additional components for the profile are used in the optimal extraction. The additional components do not share the PSF parameters and in cases where the additional component is an extended object, the fits have been inspected to ensure that the additional component does not skew the fit towards a different PSF. The additional components are not used for the weights in the extractions.

The spectra are corrected for Galactic extinction using the E(B-V) value from the dust maps of Schlegel et al. (1998) with the update in Schlafly & Finkbeiner (2011)⁵, and the extinction curve by Cardelli et al. (1989) with a total to selective extinction $R_V = 3.1$. The wavelengths of the extracted 1D-spectra are moved to vacuum, corrected for barycentric motion, and the wavelength recalibration described in Sect. 4.2 is applied. Pixels with pixel-to-pixel variation larger than 50σ are additionally added to the bad pixel map.

4.4. Telluric correction

For all earth-based telescopes, the light first has to pass through Earth's atmosphere, where the atmospheric content and conditions make an imprint on the received spectrum. These telluric features can be corrected for in a multitude of ways. We employ a prioritized list of methods here, depending on the availability of the different method. Since the observation are often taken at odd times under varying conditions, this prioritized list ensures that we are always doing the optimal correction.

The highest priority method is using the GRB afterglow continuum itself, where the atmospheric conditions have directly been imprinted on the spectrum. The telluric features can directly be fit with an atmospheric model (Smette et al. 2015; Kausch et al. 2015), which can then be used to correct for the absorption. The accuracy of the correction depends on the S/N for the target spectrum, where we have chosen the requirement that the afterglow continuum spectrum has a median signal-to-noise higher than a value of 10.

⁴ X-shooter User Manual available at <https://www.eso.org/sci/facilities/paranal/instruments/xshooter/doc.html>

⁵ Queried from <http://irsa.ipac.caltech.edu/applications/DUST/index.html> using Ginsburg et al. (2016)

If the afterglow is not sufficiently bright, telluric standard stars observed close in the time to the GRB can be used as a proxy for the atmospheric condition during the GRB observation. Here we employ the telluric correction method that has been developed in [Selsing et al. \(2015\)](#), where a library of synthetic templates is fit to the observed telluric standard.

In the last case, where the object is neither bright enough, or there for some reason have not been observed a telluric standard, we rely on the synthetic sky model by ([Noll et al. 2012](#); [Jones et al. 2013](#)) for which we generate a synthetic transmission spectrum, which we then use, where the ambient parameters for the observations have been used.

4.5. Continuum estimate

We additionally provide an estimate of the continuum for all the spectra presented here. For this, we have developed an algorithmic approach that attempts to automatically finds the continuum placement along with the error on the continuum estimate through an iterative procedure. The method is entirely data-driven and does not rely on any physical assumptions. The method is applied on each arm separately for each spectrum.

To estimate the continuum, a number of points (typically on the order of 100) are inserted at random positions along the wavelength direction, the flux-density of each point is determined by the median value of the spectrum in a small region ($\sim 1\text{\AA}$) surrounding each point. The points are fitted with a low order polynomial (we use `numpy.polynomial.chebyshev`) and iteratively, the point furthest away are removed until the polynomial fit differ from the points by less than ~ 5 per cent. This filtering is used because the afterglow continuum of GRBs are power laws ([Piran 2005](#)), and by removing points that differ significantly from a smooth continuum shape will guide the continuum estimate to a shape more reasonable for GRB afterglows. Additionally, points spaced less than around 1 per cent of the entire spectral coverage are pruned. The remaining filtered and pruned points are then spline interpolated using `scipy.interpolate.splrep;splev`, which serves as a first estimate of the continuum placement. An attempt to identify absorption and emission regions are then carried out, where they are marked as such if the difference between the estimated continuum and the observed spectrum is larger than 3 - 5 times the associated error spectrum. All regions marked as affected are then masked.

Using the masked spectrum, the entire process is then repeated 500 times where the final continuum estimate is the mean of the continuum realizations and the associated error estimate is the standard deviation. This error reflects the stability of the algorithm across the spectrum. An example of the performance is shown in Fig. 2. In some cases, very little continuum is contained in a single arm and a manual continuum estimate is provided, similar to what is done in [López et al. \(2016\)](#). In these cases the continuum error is set to 10 per cent. The code for the continuum estimate is released along with the paper at <https://github.com/jselsing/XSGRB-sample-paper>.

4.6. Spectral resolution

The afterglow spectra described in this paper are obtained in Target-of-Opportunity (override) mode. In most cases there is therefore little possibility to tweak slit widths to the seeing at the time of observations (i.e. to optimize spectral resolution and signal to noise), and almost all our data is therefore taken with

a fixed set of slit widths and binning, described above. In a fair number of cases, the seeing full width at half maximum (FWHM) is considerably smaller than the slit width, and the delivered spectral resolution will then be determined by the seeing rather than slit width, as afterglows are point sources (this is evidently not the case for extended sources, e.g for host galaxies). The delivered resolution for slit width dominated spectra post-reduction and extraction can easily be determined from the bright sky emission lines. For afterglow spectra with very high signal to noise, the delivered spectral resolution can at times be determined from the science data themselves. However, in the presence of multiple velocity components in absorption, other forms of line broadening, and a lack of lines at some redshifts, this is difficult to do at poorer signal to noise ratios (the majority of spectra in our sample). A broad starting value for the expected resolution will help fitting of these spectra, and can be important in upper limit determination, and for this reason we construct a crude relation between the seeing and the delivered resolution at our slit width, binning, and reduction pipeline settings.

To this end we use observations of telluric standard stars that are taken with identical instrument settings as our afterglow spectra, usually just after the science data, as part of the ESO X-shooter calibration plan. These spectra have been reduced together with the afterglow spectra, using identical pipeline settings with the same version of the pipeline. First we fit a Gaussian function in the spatial direction of the trace of the standard star at 792 nm (i.e. in the VIS arm). After this, we fit a series of 20 telluric absorption lines in the telluric standard star spectra with Gaussians, taking care to select transitions that are not almost-resolved multiples, should be intrinsically unresolved, and are in areas with well defined continuum flux. We pick 34 telluric standard stars spanning a range of DIMM seeing values, with the majority between $0.5 - 1.5''$. The resulting distribution of spectral FWHM (km/s) as a function of spatial FWHM at 792 nm is fairly well described by a linear relation $a + b * x$, with x the spatial FWHM in pixels (with 0.15 arc sec per pixel), $a = 21.4 \pm 1.3$ km/s, $b = 1.4 \pm 0.2$. We use this linear relation as a way to estimate the spectral resolution for medium to poor signal to noise afterglow spectra in the VIS arm. To extend this to the UVB and NIR arm, we measured a series of lines in NIR arm spectra of a subset of 19 sources used for the VIS arm above, and find that the resulting distribution is consistent with a simple scaling of the VIS arm relation by the ratio of resolutions of the NIR and VIS arm for unresolved, slit filling, sources as given on the ESO instrument website. The UVB arm contains no suitable absorption lines to use, and we therefore use a scaled value as in the NIR arm. While this simple method is not terribly accurate (for one, the spatial profile of the trace is not a perfect Gaussian), but it gives a sufficiently accurate estimate for the analysis of these poor signal to noise science spectra.

4.7. Science data products

All the spectra are made available at <http://www.dark-cosmology.dk/~jselsing/XSGRB> and additionally through the ESO archive in the form of phase 3 material⁶. This release includes the spectra of GRBs outside the statistical sample and includes both prompt afterglow observations as well as late time observations of the associated hosts and represents *all* afterglow spectra of GRBs carried out by VLT/X-shooter from the commissioning of the instrument, 14.03.2009, and until the end of the last period of the program 098.A-0055,

⁶ http://archive.eso.org/wdb/wdb/adp/phase3_main/form

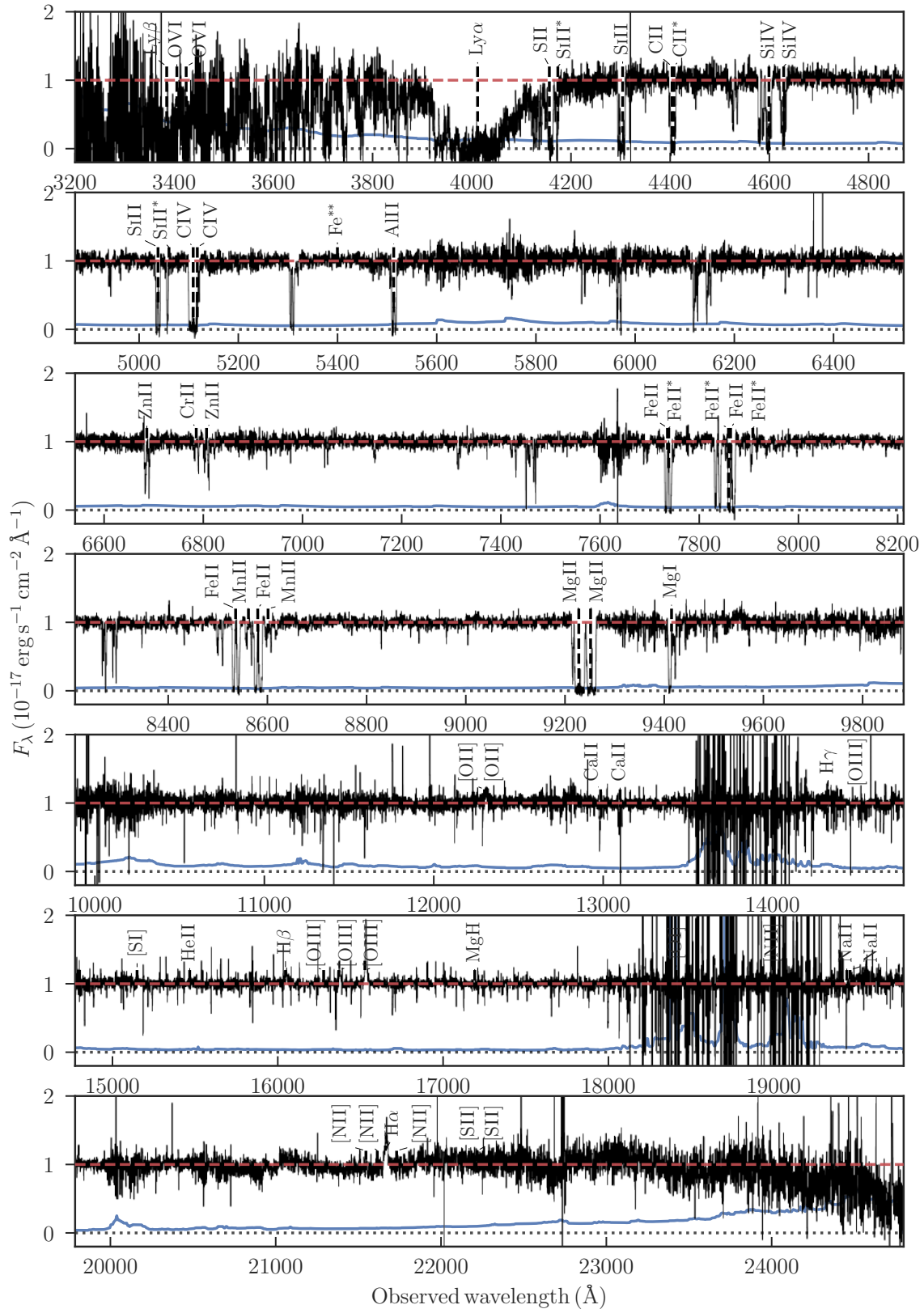


Fig. 2: Telluric corrected, normalized spectrum of GRB 121024A at $z = 2.300$, that illustrates the typical data quality. The continuum estimate is shown in dashed red and the error spectrum in solid blue. The acquisition magnitude is $r = 20$, meaning it is in the brighter end of the sample presented here, but not the brightest. The spectrum is rich in absorption, including absorption from molecular H_2 . The absorption trough visible at $\sim 4000 \text{ \AA}$ is due to $\text{Ly}\alpha$ in the host. We have overplot the most prominent lines seen in GRB afterglows from Christensen et al. (2011). Additionally, three intervening systems are seen in this sightline. This spectrum has been analyzed in detail in Friis et al. (2015).

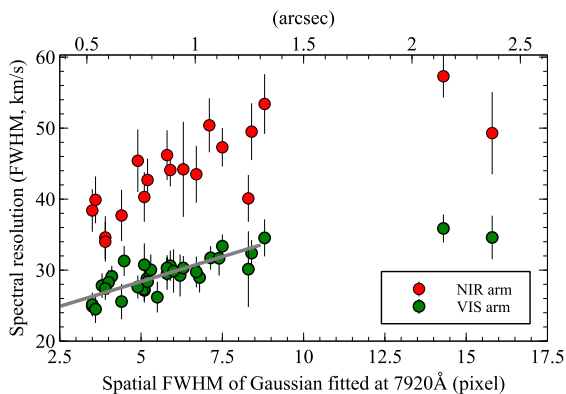


Fig. 3: Green datapoints show the FWHM (km/s) of Gaussian fits to unresolved telluric absorption lines in the VIS spectra, as a function of the FWHM of a Gaussian fit onto the trace in spatial direction at 792 nm. The lower horizontal axis is in units pixels, the top axis in arc seconds. The red datapoints show a subsample of NIR spectra. The grey line shows a linear fit to the VIS datapoints.

31.03.2017 and thus constitutes 8 years of GRB afterglow observations with VLT/X-shooter. An overview of all the spectra provided here are given in Table. 1. For each burst, each individual observation is provided in a separate reduction and in cases where observations have been repeated for an increased S/N or to follow the temporal evolution, a combined spectrum is also provided. No attempt has been made to join the spectroscopic arms, so for each observation, three spectra are provided in separate files.

All spectra are released in the ESO Science Data Product (SDP) format (Micol et al. 2016), and formatted as binary FITS files. The naming convention is based on the GRB name and the observation number, and follow the scheme GRBxxxxxxx_OBxarm.fits. For example, the visual arm of the third observation of GRB 151021A, observed in RRM mode (see Sect. 2.3), is named GRB151021A_OB3VIS.fits.

Each file contains 7 columns with following contents and descriptions:

- WAVE - Observed wavelength in vacuum, corrected for barycentric motion and drifts in the wavelength solution (Å).
- FLUX - Observed flux density ($\text{ergs}^{-1}\text{cm}^{-1}\text{Å}^{-1}$)
- ERR - Associated flux density error ($\text{ergs}^{-1}\text{cm}^{-1}\text{Å}^{-1}$)
- QUAL - Bad pixel map, where a value different from zero indicates a bad pixel.
- CONTINUUM - Continuum estimate based on Sect. 4.5 ($\text{ergs}^{-1}\text{cm}^{-1}\text{Å}^{-1}$)
- CONTINUUM_ERR - Relative error on the continuum estimate
- TELL_CORR - Inverse transmission spectrum. Multiply FLUX and ERR column with this column to correct for telluric absorption.

5. Results

In this section, we describe the successfulness of the follow-up effort and the characteristics of the observed bursts. We also assess the degree to which the obtained sample is representative for the full *Swift* sample. An important note is that here we include *all* GRB after 14.03.2009, that have been observed with

X-shooter, while only a subset of these constitute our *statistical* sample. The statistical sample is based on the selection criteria described in Sect. 2.1. Some bursts not fulfilling the sample criteria have been followed up due to interesting characteristics, e.g. curiosity properties of their light curves, their brightness, etc. These bursts are not discussed as part of the investigation of the statistical properties of the GRB population. A prime example of a burst outside the statistical sample is bright INTEGRAL burst GRB 161023A, that turned to be a rich spectrum with at least 11 intervening absorption systems.

5.1. Follow-up timing and afterglow brightness

Redshift determination of bursts for which the host is too faint for a spectroscopic redshift measurement relies on the detection of absorption line imprinted on the GRB afterglow continuum. Because the afterglow rapidly fades (typically as $\sim t^{-1}$) a rapid follow-up is essential. In Fig. 4 we plot the delay from the BAT trigger to the start of the spectroscopic observation. The shortest delays are observed in RRM-mode. The fastest follow-up between BAT trigger and start of spectroscopic observations in our sample is for the short, $z = 1.717$, GRB 160410A for which spectroscopic integration was initiated only 8.4 minutes after the BAT trigger. To illustrate importance of the follow-up delay for the redshift completeness, we plot the redshift completeness as a function of delay time in Fig. 4 for all the bursts we have followed up, including the ones outside the statistical sample. Visible is the decreasing fraction of GRBs with a redshift determination for increasing delays. The overall redshift completeness for bursts that we have followed up is 92 per cent. This degree of completeness in the followed bursts, illustrates the efficiency of VLT/X-shooter in redshift determination. Not shown in the figure are an additional 12 bursts that have redshift determinations based on late-time host observations with delay times longer than ~ 10 days.

5.2. Sample completeness

Based on the sample criteria specified in Sect. 2.1, a total of 158 bursts have triggered *Swift* in the period since the commissioning of VLT/X-shooter. This sample constitutes the *statistical sample* from which we will derive statistical properties of the GRB population. The redshift completeness of the full statistical sample is 60 per cent. We return to the question of redshift completeness in Sect. 5.4. From this sample, 90 GRBs have been spectroscopically followed up with X-shooter. In order to assess whether the subset of bursts followed up are representative of the underlying GRB parent population, we compare intrinsic properties of GRBs in our sample to GRBs in the full sample followed up by *Swift*. We show the comparison between the BAT (15-150 keV) fluence, the XRT flux (0.3 - 10 keV) at 11 hours, and the intrinsic X-ray derived equivalent hydrogen column density, $N_{\text{H},\text{X}}$, in Fig. 5. For the latter, we can only use values of $N_{\text{H},\text{X}}$ derived for bursts with a measured redshift, excluding ~ 75 per cent of the bursts. We return to this last point in Sect. 5.5.

Using the observational characteristics of the 1322 bursts observed by 24.10.2017 by *Swift*, and $N_{\text{H},\text{X}}$ (Evans et al. 2009), we can quantify the degree to which our sample is biased relative to the overall *Swift* sample. The values are queried from the online *Swift* database^{7,8}. Three samples are of interest in order to assess the completeness of the follow-up campaign (Fig. 5); the

⁷ http://swift.gsfc.nasa.gov/archive/grb_table/

⁸ http://www.swift.ac.uk/xrt_live_cat/

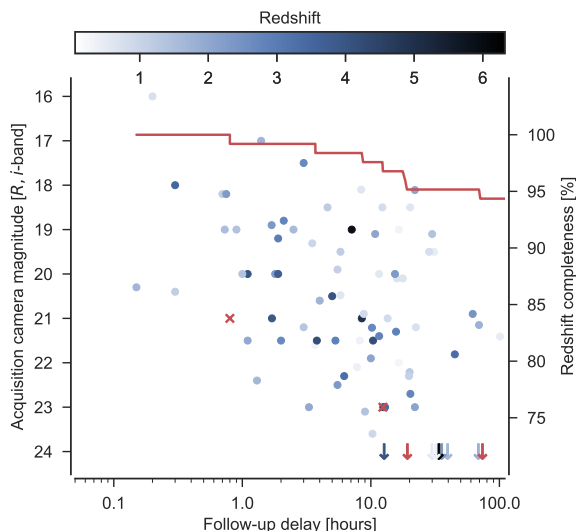


Fig. 4: afterglow magnitude at the start of observation as a function of follow-up delay. The points have been colored based on the redshift of the corresponding burst. Red crosses indicate GRBs without a measured redshift and arrows indicate bursts for which the afterglow was not detected in the acquisition image. In red is shown the redshift completeness as a function of follow-up delay.

full *Swift* sample consisting of all the bursts observed by *Swift* (blue), all the bursts that fulfill the selection criteria imposed in Sect. 2.1 (green), and the bursts actually followed up with X-shooter (red).

For each of the samples, we calculate the median, 14th, and 86th percentiles of each of the distributions, which can be used as point estimates for the population distribution. These are provided in Table. 2. It can be seen from the values that the three samples have very similar distributions in terms of the point estimates chosen. This suggests that our selection criteria are unbiased compared to the *Swift*-sample and that additionally, the follow-up effort conserves the distributions of the intrinsic GRB properties (except perhaps for $N_{\text{H,IX}}$, see Sect. 5.5).

Additionally, using a 2-sided Kolmogorov-Smirnov test (KS-test), we can assess the degree to which the null, that the two distributions are drawn from the same parent distribution, can be rejected. We show a graphic representation of the test statistics in Fig. 6. A high p-value indicates little evidence against the null, meaning for the properties investigated here. The distribution of $N_{\text{H,IX}}$ exhibits the highest degree of dissimilarity, but the two distribution are still consistent with being drawn from the same underlying distribution.

We therefore conclude that the statistics of the sample presented here, conserves the intrinsic properties of the GRBs in the full *Swift* sample. At least in terms of BAT fluence and X-ray afterglow flux at 11 hours.

5.3. Properties of rejected triggers

Out of the 158 bursts in the statistical sample, 32 (~ 20 percent) have not been observed due to reasons unrelated to the GRB or afterglow properties. The reasons includes unavailability of the telescope due to technical maintenance (e.g., mirror re-coating),

a visitor rejecting the TOO trigger, or bad weather. Because this cut is unrelated to the GRB properties, it will not change the statistical properties of the full sample. Removing all these bursts, drastically improves the redshift completeness from 60 per cent to 83 per cent.

5.4. On the redshift distribution of GRBs

One of the objectives of our follow-up campaign is to measure the redshift distribution for a well-defined, observationally unbiased and statistical useful sample of GRBs. The imposed selection criteria (see Sect. 2.1) ensure that the GRBs entering our homogeneous sample fairly represent the underlying population. The redshift distribution of such a sample holds valuable information about the occurrence of GRBs through cosmic time (Jakobsson et al. 2012; Perley et al. 2016a).

In Fig. 7 we show the redshift distribution of all the observed GRBs. In the top panel we show a histogram for the full sample and the statistical sample and in the main panel, we show the redshifts of the individual bursts as a function of GRB luminosity in the observed 15-150 keV band. To calculate the luminosity, L_{BAT} , we follow a similar procedure as Lien et al. (2016) and define $L_{\text{BAT}} = F_{\gamma} 4\pi d_L^2 (1+z)^{-1}$, where F_{γ} is the observed BAT fluence in the 15-150 keV band and d_L is the luminosity distance to the burst at the given redshift. Note that this measure of luminosity does not include any k-correction. As an indication of the effect of the *Swift* sensitivity limit on the redshift distribution, also in the figure, we have shown the so called ~ 1 s flux BAT sensitivity limit ($\sim 3 \times 10^{-8} \text{ erg s}^{-1} \text{ cm}^{-2}$; Baumgartner et al. 2013; Lien et al. 2016). Due to complex triggering mechanism of *Swift*, this sensitivity limit should be interpreted with some caution as the effective limit depends on the light curve of the prompt emission signal. Due to the dilution of light with distance, the *Swift* GRB luminosity detection limit is almost an order of magnitude brighter at $z = 2$ than at $z = 1$. At $z \geq 4$ we are only able to observe GRBs that are ~ hundred times brighter than the faintest bursts at $z = 1$ and below.

We find the following mean and median and 14th and 86th percentiles for the redshift distribution. First for the statistical sample: $z_{\text{avg}} = 1.99$, $z_{\text{med}} = 1.64$, $z_{14\%} = 0.60$ and $z_{86\%} = 3.39$. For all GRBs observed with X-shooter we find $z_{\text{avg}} = 1.90$, $z_{\text{med}} = 1.52$, $z_{14\%} = 0.55$ and $z_{86\%} = 3.36$. For comparison, the corresponding values found in Fynbo et al. (2009) are $z = 2.2$ for both the mean and the median.

Because the redshift completeness of our statistical sample is 60 per cent, making inference of the *true* redshift distribution of GRBs on this sample is difficult. The biases introduced in the redshift distribution by the increased ability to secure redshift of optically brighter bursts has been investigated by Turpin et al. (2016) which find that we systematically find redshift for longer GRBs. Additionally only the brightest GRBs are seen above redshift $z \gtrsim 1$ as shown in Fig. 7. Additionally, as described in detail in Perley et al. (2016b), bursts for which the redshift is measured from the afterglow are systematically found for host galaxies with a lower luminosity than burst for which the redshift is measured from the host galaxy. Only a few GRBs hosted in galaxies more massive than $10^{10} M_{\odot}$ have the redshift measured based on the afterglow continuum.

5.5. Sample darkness

A large fraction of all GRBs exhibit no detectable or very faint optical afterglows (Groot et al. 1998; Djorgovski et al. 2001;

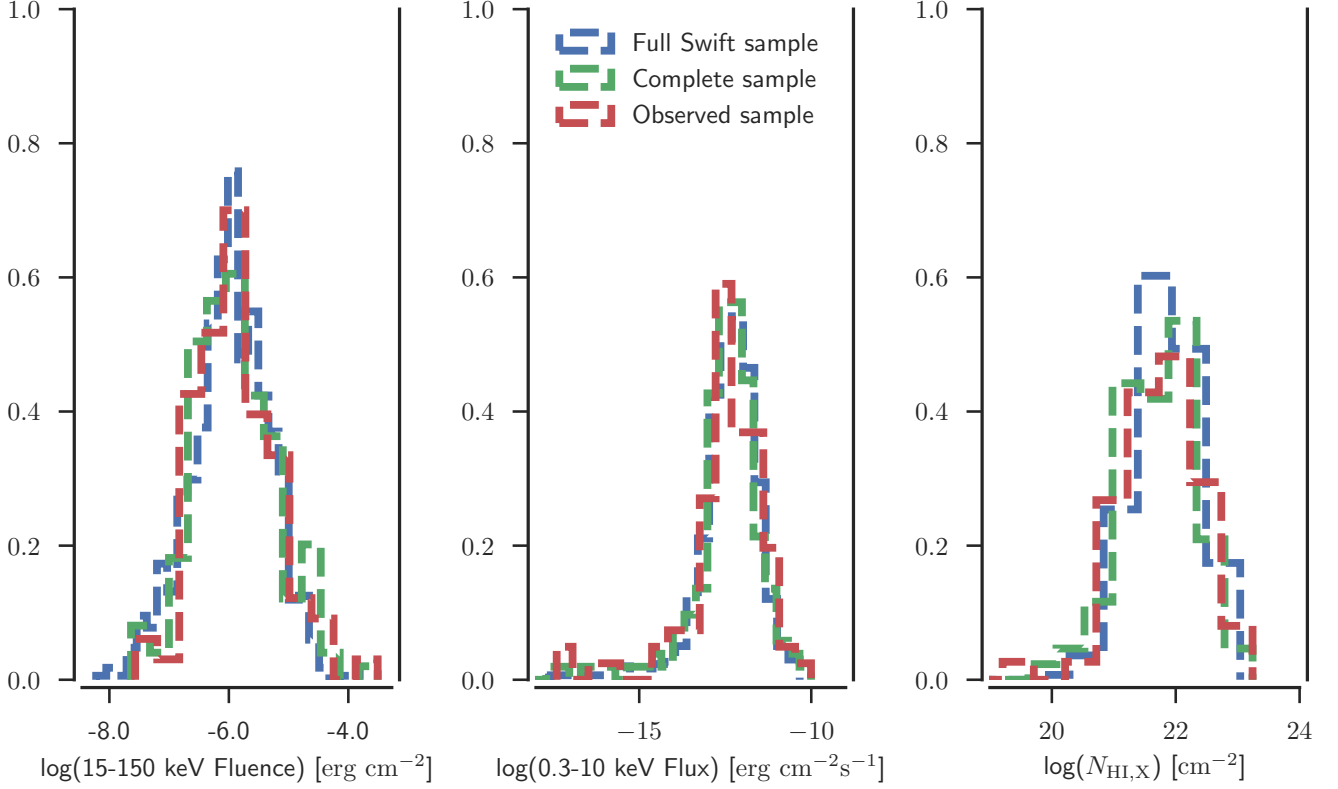


Fig. 5: Comparison between burst properties of all bursts observed with *Swift* (blue), the ones that fulfill the sample criteria specified in Sect. 2.1 (green), and the subset that has been observed as part of the statistical sample (red). The left plot shows the fluence in range 15-150 keV as observed by BAT. The middle panel shows the 0.3 - 10 keV flux, 11 hours after the bursts as measured by XRT. In the right most panel, we show $N_{\text{HI,X}}$ based on the XRT spectrum (Evans et al. 2009).

	Full <i>Swift</i> sample	Statistical sample	Followed up bursts
N_{BAT}	987	156	89
$\log(15 - 150\text{keV fluence})$	$-5.9^{+0.7}_{-0.6}$	$-5.9^{+0.7}_{-0.6}$	$-5.9^{+0.7}_{-0.7}$
N_{XRT}	909	154	88
$\log(0.3 - 10\text{keV flux})$	$-12.3^{+0.7}_{-0.8}$	$-12.4^{+0.7}_{-0.8}$	$-12.4^{+0.9}_{-0.7}$
$N_{\text{HI,X}}$	250	95	74
$\log(N_{\text{HI,X}})$	$21.7^{+0.6}_{-0.9}$	$21.5^{+0.7}_{-3.4}$	$21.6^{+0.7}_{-4.5}$

Table 2: Population properties (median and 14th and 86th percentiles as the error intervals) for the *Swift sample* and the subset of bursts fulfilling the sample criteria. The population characteristics of the three samples are very similar, which shows that our selection criteria effectively conserve the statistical properties of the underlying population, as least for these parameters.

Fynbo et al. 2001). The degree of optical extinction relative to the X-ray brightness has been parametrized in term of their optical darkness, β_{OX} (Jakobsson et al. 2004; Rol et al. 2005; van der Horst et al. 2009). The X-ray properties of such bursts has previously been investigated (De Pasquale et al. 2003; Fynbo et al. 2009; Melandri et al. 2012). There is some indications that dark bursts have somewhat higher X-ray luminosity and $\log(N_{\text{HI,X}}/\text{cm}^{-2})$ compared to the optically brights bursts. This indicates along with investigations of host galaxy properties (Greiner et al. 2011; Krühler et al. 2011; Hjorth et al. 2012; Perley et al. 2016b), that the extinction of the optical afterglow is primarily driven by the presence of dust in the host galaxy.

For all bursts with follow-up within 100 hours we calculate the "darkness"-parameter, β_{OX} (Jakobsson et al. 2004). This requires the simultaneous measurement of the X-ray flux density

and the optical flux density which is in practice never possible. As a proxy, we use the measured acquisition camera magnitude reported in Tab. 1 to get the optical flux density at the beginning of the spectroscopic integration. Because we know the delay between the follow-up and the *Swift* trigger, we can use the measured XRT lightcurve (Evans et al. 2007, 2009)⁹ to infer the corresponding X-ray flux density at the time of the optical observation. This is done by either linearly interpolating between temporally neighboring XRT measurements or by extrapolating the last few X-ray data points to the spectroscopic delay. When the afterglow is not detected in the acquisition camera, an upper limit of > 24 mags is used, which propagates into an upper limit on β_{OX} .

⁹ http://www.swift.ac.uk/xrt_curves/trigger_numer/flux.qdp

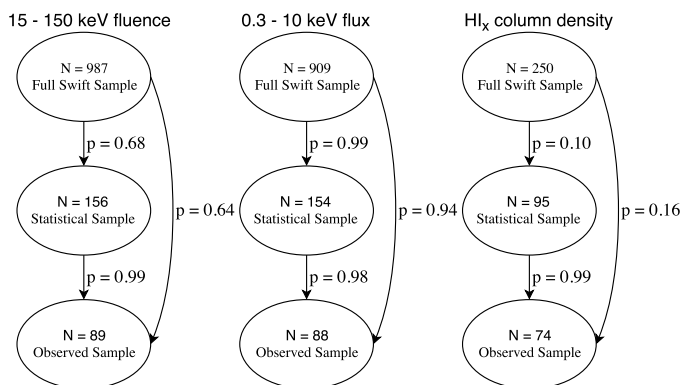


Fig. 6: Relational graph shown the respective p-values that the different sample are drawn from the same underlying distribution. The arrows represent the comparison with each of the p-values are listed next to. Only in the HI column density distribution is there mild evidence against the null, but the discrepancy is mainly driven by a relatively larger fractional contribution from low-column hosts.

In Fig. 8 we compare the $\beta_{\text{OX}} - N_H$ distribution with the one presented in Fynbo et al. (2009). The values from Fynbo et al. (2009) have been treated as detections, meaning that we artificially bias the distribution towards higher β_{OX} -values. We tentatively confirm the result by Fynbo et al. (2009), that dark bursts, $\beta_{\text{OX}} < 0.5$, have higher $\log(N_{\text{H,IX}}/\text{cm}^{-2})$. Specifically, for bursts with measured redshift either from the afterglow or the host galaxy, we find the following: For bursts with $\beta_{\text{OX}} \geq 0.5$ we find $\log(N_H) = 21.4^{+0.7}_{-1.0}$, whereas for $\beta_{\text{OX}} < 0.5$ we find $21.8^{+0.5}_{-0.9}$ where 68 per cent of the probability mass is contained within the error intervals. A 2-sided KS test fails to reject the null that they are drawn from the same distribution with $p = 0.43$, meaning there is not strong evidence for a discrepancy.

It is clear, however, that the fraction of dark bursts for which we have measured the redshift is lower than the intrinsic dark burst fraction. To measure the redshift as we either need a detected afterglow to obtain a spectrum or to locate the host galaxy and determine the redshift from there. It is more difficult to correctly associate a galaxy with a burst when there is no detected optical afterglow and hence a correct redshift measurement is more difficult to make, see Jakobsson et al. (2005); Levesque et al. (2010) and Perley et al. (2017) for a recent example.

Using the table maintained by Greiner¹⁰, we can see how the presence of an optical afterglow affects the follow-up statistics. 50.5 percent of all *Swift*-detected bursts do not have an detected optical afterglow, but this number also includes bursts where no optical observations were available, so is a lower limit. For the bursts entering our statistical sample, the number of bursts without a detected optical afterglow is ~ 27 percent, close to the upper limit on the fraction of dark bursts found in a complete sample with a very high degree of redshift completeness (Melandri et al. 2012). Of the bursts for which follow-up has actually been attempted, this number is ~ 18 percent, confirming that we are indeed biased against bursts without a detected optical afterglow in the spectroscopic sample.

Despite that the fraction of dark bursts is lower in the observed sample, compared to the statistical sample, the X-ray properties not differ significantly, as shown in Sect. 5.2. If the tendency for dark bursts to have a higher $\log(N_{\text{H,IX}}/\text{cm}^{-2})$ is

real, that the decreased fraction of dark bursts does not alter the observed prompt X-ray brightness distribution, potentially reflects the independence of the X-ray brightness on the density of the circumburst medium (Freedman & Waxman 2001; Berger et al. 2003; Nysewander et al. 2009), if the measured $\log(N_{\text{H,IX}}/\text{cm}^{-2})$ is primarily driven by a high column local to the burst. Because we only use values of $\log(N_{\text{H,IX}}/\text{cm}^{-2})$ in the comparison for which the GRB has a measured redshift, this measure is likely biased toward optically brighter bursts.

Since *all* GRBs should have an optical afterglow, the presence of an optical afterglow is more a statement about the sensitivity than optical properties of the bursts.

This is despite spectroscopic follow-up only being carried out in cases where either a detectable optical afterglow or a clear counterpart are seen, which naively should be biased against dark bursts occurring in more obscured galaxies, which is shown to exhibit different galactic properties (Perley et al. 2009; Krühler et al. 2011; Rossi et al. 2012; Perley et al. 2013, 2015).

5.6. Hydrogen column densities

Because the locations of long GRBs are associated with intensely star forming regions (Hogg & Fruchter 1999; Bloom et al. 2002; Fruchter et al. 2006), the GRB afterglow light has to propagate through the large amounts of hydrogen fueling the star formation. Because a significant fraction of the hydrogen has not been ionized yet, the optical depth at the wavelength of $\text{Ly}\alpha$ is very high, saturating not only the line center, but also the damping wings. This causes a strong absorption system to appear in the afterglow continuum. For bursts with $z \gtrsim 1.7$, the position of $\text{Ly}\alpha$ moves into the spectroscopic coverage of X-shooter, meaning that we are able to detect this absorption trough due to $\text{Ly}\alpha$.

Due to the stochastic nature of the $\text{Ly}\alpha$ -forest, the blue wing of the Lyman- α absorption line is randomly superposed with Lyman- α forest systems, along with strong absorption from Mn II and Si III, making it notoriously difficult to model. Additionally, the red wing has got the ISM signatures imprinted on it, especially strong absorption due to Si II, [S II] and [N V], which can exhibit significant velocity structure. Along with instrumental effects, the generative model for the data that we would use in a likelihood-based analysis would be very complicated, we have decided not to make formal χ^2 fitting of the hydrogen column densities, but instead use a more subjective visual fitting to the absorption profile. Using an analytic approximation to the absorption profile from (Tepper García 2006), we overplot a synthetic absorption line with a specified column density on our observed, normalised spectrum. By tuning the value of the hydrogen column density until the synthetic absorption line matches the spectrum, we can thereby infer the actual column densities of the GRB sight line in a manual way. In a similar fashion, the errors on the hydrogen column can be estimated. We show the results of this procedure for all bursts where possible in Fig. 10 and the inferred hydrogen column densities in Table 3

In the compilation of HI measurements towards GRBs in ? there are 81 published HI values. We here provide 39 new HI column density measurements, i.e. an increase of the number of optically derived hydrogen column densities of ~ 50 percent. We compare the median, the 14th, and 86th percentiles of the two distributions where the sample presented here has $21.8^{+0.3}_{-0.8}$ and the rest of the literature values has $21.5^{+0.4}_{-1.5}$. We see that the two distribution has a large degree of overlap due to the large width of the distributions, but we find a slightly higher median value for the new sample presented here. A 2-sided KS test gets us a p-

¹⁰ <http://www.mpe.mpg.de/jcg/grbgen.html>

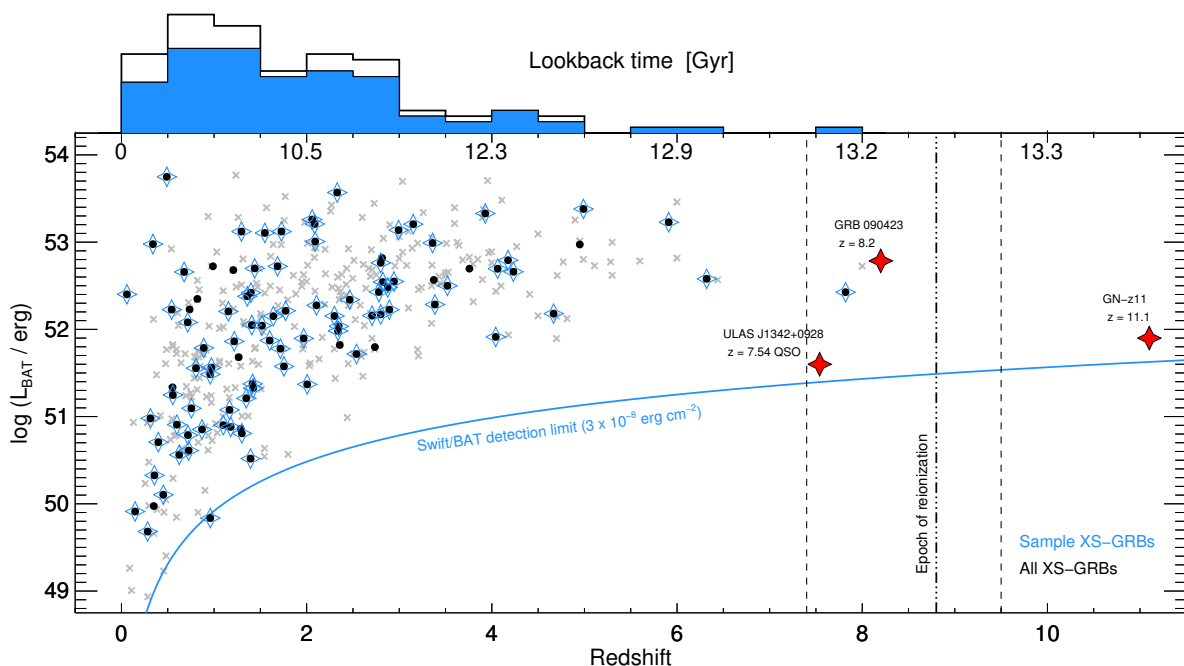


Fig. 7: Redshift distribution as a function of intrinsic BAT γ -ray luminosity, L_{BAT} . Bursts that are a part of the statistical sample are marked by blue stars and black dots show all GRBs observed with X-shooter. All *Swift* GRBs with measured redshifts is shown in grey. For comparison, we overplot with red stars the GRB (Tanvir et al. 2009; Salvaterra et al. 2009), quasar (Bañados et al. 2017), and galaxy (Oesch et al. 2016) with the highest spectroscopically confirmed redshifts, the latter two shown at arbitrary L_{BAT} . The blue solid line represents so-called 1 s BAT sensitivity limit described in the text. The estimated epoch of reionization is shown by the black dot-dashed line, with the uncertainty shown as the black dashed lines, from the most recent measurement by Planck Collaboration et al. (2016).

value of $p = 0.006$, meaning relatively large evidence against the null that the two samples are drawn from the same underlying distribution. Because the bursts that have measurements of the hydrogen column density are selected solely based on our ability to infer a column, it is difficult to make any strong conclusions about the population statistics in terms of gas content.

We show the comparison between the two samples in Fig. 9. We additionally show the column-distribution for 12081 quasar DLAs from Noterdaeme et al. (2012). The fact that GRBs systematically are located behind the highest $\log(N_{\text{HI}}/\text{cm}^{-2})$, previously noted by (e.g., Prochaska et al. 2007; Fynbo et al. 2009), is striking. The reason for this is that quasars sampling of sightlines through galaxies is cross-section selected, whereas GRB sightlines probe more central, dense regions in their hosts.

6. Discussion and conclusions

In this paper we have presented the results of a dedicated effort over the years 2009 – 2017 to use the X-shooter spectrograph on the ESO-VLT to secure spectroscopic observations of afterglows and host galaxies of GRBs detected by *Swift*. This work was initiated by a consortium using Guaranteed Time on X-shooter, but over the years the project continued in open time and the team was opened to include any researchers interested in contribution to this effort.

The sample we present here include spectroscopic observations of 90 systems fulfilling our sample criteria including 17 spectra that are late time observations of the underlying host galaxies. All spectra have been made publicly available in the reduced form used in this paper.

Our sample serves the purpose to further characterize the environments of GRBs that was also much advanced by the previous surveys based primarily on lower-resolution spectrographs. The most striking result found is that GRBs typically are located behind very large column densities of neutral hydrogen. Only after observing more than 12000 damped Lyman- α absorbers (DLAs) towards about 10^5 quasars have a handful such systems with $\log(N_{\text{HI}}/\text{cm}^{-2}) > 22$ been identified (e.g., five in Noterdaeme et al. 2012). Long GRB afterglow spectra, by contrast, reveal such systems in the majority of cases (Jakobsson et al. 2006; Fynbo et al. 2009; Cucchiara et al. 2015, and this work). With afterglow spectroscopy (throughout the electromagnetic spectrum from X-rays to the sub-mm) we hence characterize the properties of star-forming galaxies over cosmic history in terms of redshifts, metallicities, molecular contents, ISM temperatures, UV-flux densities, extinction curves, etc. A number of independent papers have been published or submitted for publication focusing on many of these specific issues of our sample such as extinction curves (Japelj et al. 2015; ?, see also Fynbo et al. 2014; Heintz et al. 2017c), emission lines from the underlying host galaxies (Krühler et al. 2015), the frequency of intervening Mg II absorbers (Christensen et al. 2017), and escape of ionizing radiation (Tanvir et al. in prep).

It seems important to end this paper by stressing that the potential of using GRB sightlines as probes is far from fully harvested. The sample of sightlines probed by our spectra is not representative for all GRB sightlines as we have shown and consistent with earlier findings from samples based on low-resolution spectroscopy (e.g., Fynbo et al. 2009) and from studies of complete samples of GRB host galaxies (Hjorth et al. 2012; Covino et al. 2013; Perley et al. 2016c). Krühler et al. (2013) convinc-

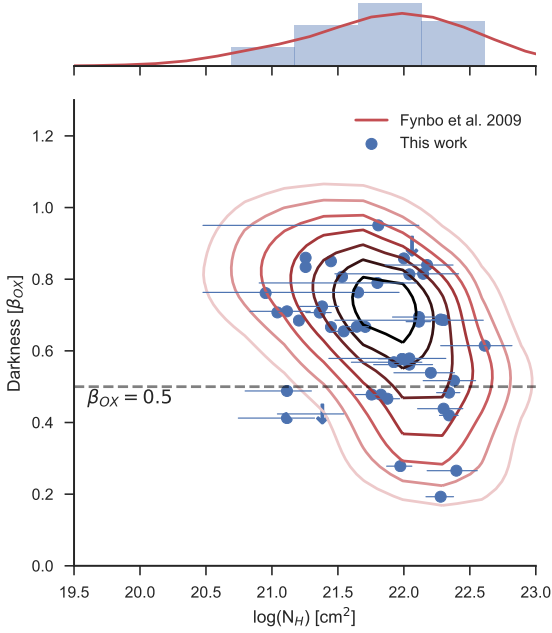


Fig. 8: Optical extinction relative to X-ray against X-ray derived hydrogen column densities. In red is shown the sample presented in Fynbo et al. (2009) where lines indicate the kernel density estimate of the distribution where limits have been replaced with values. We note that contrary to what is presented in Fynbo et al. (2009), we exclude all bursts for which we do not have a redshift. Darker colors represented higher density of points. The corresponding marginal distributions are shown. In blue is the points for the bursts presented here along with the marginal histograms. Limits on β_{OX} is shown by downwards facing arrows.

ingly argue, that very rich sightlines like that probed by the remarkable GRB 080607 (Prochaska et al. 2009) are probably significantly more frequent than in the sightlines sampled by our spectra. However, with current instrumentation these sightlines are out of reach except under very fortunate circumstances as in the case of GRB 080607 when the afterglow could be observed only a few minutes after the burst with a 10-m class telescope. Observations of such sightlines with X-shooter-like spectrographs on the next generation of 20–40-m telescopes is likely to be very rewarding.

Acknowledgements. *** We should add an ode to Neil Gehrels here ***. JPUF, BMJ and DX acknowledge support from the ERC-StG grant EGG-278202. The Dark Cosmology Centre is funded by the Danish National Research Foundation. TK acknowledges support by the European Commission under the Marie Curie Intra-European Fellowship Programme in FP7. AdUP acknowledges support by the European Commission under the Marie Curie Career Integration Grant programme (FP7-PEOPLE-2012-CIG 322307). This work made use of data supplied by the UK *Swift* Science Data Centre at the University of Leicester. Finally, we acknowledge expert support from the ESO staff at the Paranal and La Silla observatories in obtaining these target of opportunity data.

References

Abrarov S. M., Quine B. M., 2015a, *J. Math. Res.*, 7, 44
 Abrarov S. M., Quine B. M., 2015b, *J. Math. Res.*, 7, 163
 Axelsson M., et al., 2012, *Astrophys. J. Lett.*, 757, L31
 Bañados E., et al., 2017, *Nature*
 Band D. L., 2006, *ApJ*, 644, 378
 Barthelmy S. D., 2000, in AIP Conf. Proc., AIP, pp 731–735, doi:10.1063/1.1361631, <http://scitation.aip.org/content/aip/proceeding/aipcp/10.1063/1.1361631>

Table 3: Hydrogen column densities for all bursts exhibiting Ly α absorption in the spectral coverage of X-shooter. The corresponding measurements are shown in Fig. 10.

GRB	Hydrogen Column
GRB 090809A	21.7 ± 0.2
GRB 090926A	21.55 ± 0.10
GRB 100219A	21.20 ± 0.20
GRB 100425A	21.0 ± 0.2
GRB 100728B	21.2 ± 0.5
GRB 110128A	21.90 ± 0.15
GRB 110818A	21.9 ± 0.4
GRB 111008A	22.40 ± 0.10
GRB 111107A	21.0 ± 0.2
GRB 120119A	22.6 ± 0.2
GRB 120327A	22.0 ± 0.05
GRB 120404A	20.7 ± 0.3
GRB 120712A	19.95 ± 0.15
GRB 120716A	21.80 ± 0.15
GRB 120815A	22.10 ± 0.10
GRB 120909A	21.75 ± 0.10
GRB 121024A	21.85 ± 0.10
GRB 121027A	22.8 ± 0.3
GRB 121201A ^a	22.0 ± 0.3
GRB 121229A	21.8 ± 0.2
GRB 130408A	21.8 ± 0.1
GRB 130427B	21.9 ± 0.3
GRB 130606A	19.91 ± 0.02
GRB 130612A	22.1 ± 0.2
GRB 131011A	22.0 ± 0.3
GRB 131117A	20.0 ± 0.3
GRB 140311A	22.40 ± 0.15
GRB 140430A	21.8 ± 0.3
GRB 140515A	19.0 ± 0.5
GRB 140614A	21.6 ± 0.3
GRB 141028A	20.6 ± 0.15
GRB 141109A	22.1 ± 0.1
GRB 150206A	21.7 ± 0.4
GRB 150403A	21.8 ± 0.2
GRB 150915A ^a	21.2 ± 0.3
GRB 151021A ^a	22.3 ± 0.2
GRB 151027B	20.5 ± 0.2
GRB 160203A	21.75 ± 0.10
GRB 160410A ^b	21.2 ± 0.2
GRB 161014A	21.4 ± 0.3
GRB 161023A	20.96 ± 0.05

Notes. ^(a) Has Ly α emission in the trough. ^(b) Short burst.

Barthelmy S. D., et al., 2005, *SSRv*, 120, 143
 Baumgartner W. H., Tueller J., Markwardt C. B., Skinner G. K., Barthelmy S., Mushotzky R. F., Evans P. A., Gehrels N., 2013, *Astrophys. Journal, Suppl. Ser.*, 207, 19
 Benner D. C., Rinsland C. P., Devi V. M., Smith M. A. H., Atkins D., 1995, *JQSRT*, 53, 705
 Berger E., Kulkarni S., Frail D., 2003, *ApJ*, 590, 379
 Berger E., Fong W., Chornock R., 2013, *ApJ*, 774, L23
 Bloom J. S., Kulkarni S. R., Djorgovski S. G., 2002, *AJ*, 123, 1111
 Briggs M. S., et al., 1996, *ApJ*, 459, 40
 Bufano F., et al., 2012, *ApJ*, 753, 67
 Burrows D. N., et al., 2005, *SSRv*, 120, 165
 Burrows D. N., et al., 2007, in SPIE Conf. Ser., International Society for Optics and Photonics, p. 668607, doi:10.1117/12.735130
 Cardelli J. a., Clayton G. C., Mathis J. S., 1989, *ApJ*, 345, 245
 Castro-Tirado A. J., et al., 2010, *A&A*, 517, A61

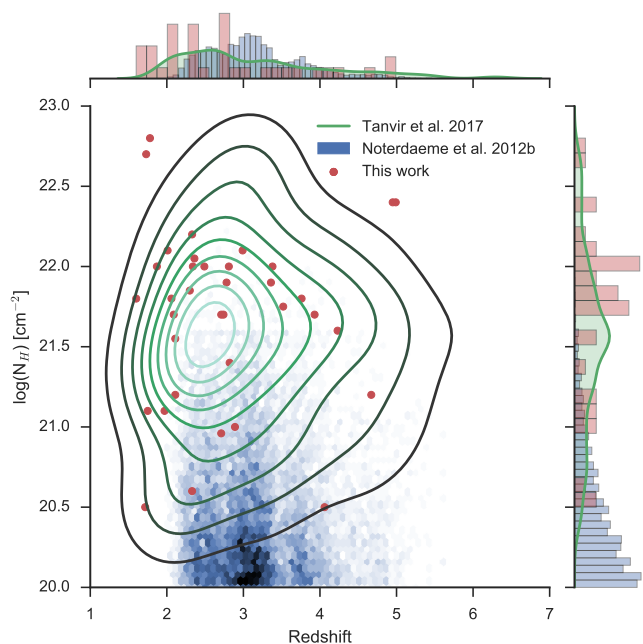


Fig. 9: Distributions of DLA hydrogen column densities for DLAs found in quasar absorption lines, from (Noterdaeme et al. 2012) in blue. Overplot in green is the kernel density estimate is the similar distribution, only for DLAs in GRB sightlines. Values are taken from the compilation in Tanvir2017 et al. (in prep), along with the new values presented in this sample. The marginal distributions for the two distribution are also shown along the left side and on the top, where the different environments probed are clearly visible in the hydrogen column densities, as previously also noted in Fynbo et al. (2009)

Christensen L., Fynbo J. P. U., Prochaska J. X., Thöne C. C., de Ugarte Postigo A., Jakobsson P., 2011, *ApJ*, 727, 73
Christensen L., et al., 2017, eprint arXiv:1709.01084
Cobb B. E., Bloom J. S., Perley D. A., Morgan A. N., Cenko S. B., Filippenko A. V., 2010, *ApJ*, 718, L150
Covino S., et al., 2013, *MNRAS*, 432, 1231
Coward D. M., Howell E. J., Branchesi M., Stratta G., Guetta D., Gendre B., Macpherson D., 2013, *MNRAS*, 432, 2141
Cucchiara A., Fumagalli M., Rafelski M., Kocovski D., Prochaska J. X., Cooke R. J., Becker G. D., 2015, *ApJ*, 804, 51
D'Elia V., Stratta G., 2011, *A&A*, 532, A48
D'Elia V., et al., 2010, *A&A*, 523, A36
D'Elia V., et al., 2014, *A&A*, 564, A38
De Pasquale M., et al., 2003, *ApJ*, 592, 1018
De Ugarte Postigo A., Thöne C. C., Goldoni P., Fynbo J. P. U., 2011, *AN*, 332, 297
Dessauges-Zavadsky M., Chen H.-W., Prochaska J. X., Bloom J. S., Barth A. J., 2006, *ApJ*, 648, L89
Djorgovski S. G., Frail D. A., Kulkarni S. R., Bloom J. S., Odewahn S. C., Diercks A., 2001, *ApJ*, 562, 654
Evans P. A., et al., 2007, *A&A*, 469, 379
Evans P. A., et al., 2009, *MNRAS*, 397, 1177
Filippenko A. V., 1982, *PASP*, 94, 715
Fiore F., et al., 2005, *ApJ*, 624, 853
Fong W., et al., 2013, *ApJ*, 769, 56
Freedman D. L., Waxman E., 2001, *ApJ*, 547, 922
Freudling W., Romaniello M., Bramich D. M., Ballester P., Forchi V., García-Dabó C. E., Moehler S., Neeser M. J., 2013, *A&A*, 559, A96
Friis M., et al., 2015, *MNRAS*, 451, 167
Fruchter A. S., et al., 2006, *Nature*, 441, 463
Fynbo J. U., et al., 2001, *A&A*, 369, 373
Fynbo J. P. U., et al., 2009, *ApJS*, 185, 175
Fynbo J. P. U., et al., 2014, *A&A*, 12, 1
Gehrels N., et al., 2004, *ApJ*, 611, 1005
Gehrels N., Ramirez-Ruiz E., Fox D., 2009, *ARA&A*, 47, 567

Ghirlanda G., 2007, *R. Soc. London Philos. Trans. Ser. A*, 365, 1385
Ginsburg A., et al., 2016, *Astroquery* V0.3.1, doi:10.5281/ZENODO.44961, <https://github.com/astroquery/astroquery>
Goldoni P., Royer F., François P., Horrobin M., Blanc G., Vernet J., Modigliani A., Larsen J., 2006, *Ground-based Airborne Instrum. Astron. Ed. by McLean*, 6269, 80
Graff P. B., Lien A. Y., Baker J. G., Sakamoto T., 2016, *ApJ*, 818, 55
Greiner J., et al., 2011, *A&A*, 526, A30
Greiner J., et al., 2015, *Nature*, 523, 189
Groot P. J., et al., 1998, *ApJ*, 493, L27
Hamuy M., Suntzeff N. B., Heathcote S. R., Walker A. R., Gigoux P., Phillips M. M., 1994, *PASP*, 106, 566
Hartoog O. E., et al., 2013, *MNRAS*, 430, 2739
Hartoog O. E., et al., 2015, *A&A*, 580, A139
Heintz K. E., et al., 2017a, *MNRAS*, 000, 1
Heintz K. E., et al., 2017b, *A&A*, 601, A83
Heintz K. E., et al., 2017c, *Astron. Astrophys. Vol. 601, id.A83*, 10 pp., 070318, 1
Hjorth J., Bloom J. S., 2011, *AIP Conf. Proc.*, p. 29
Hjorth J., et al., 2012, *ApJ*, 756, 187
Hogg D. W., Fruchter A. S., 1999, *ApJ*, 520, 54
Horne K., 1986, *PASP*, 98, 609
Jakobsson P., Hjorth J., Fynbo J. P. U., Watson D., Pedersen K., Björnsson G., Gorosabel J., 2004, *ApJ*, 617, L21
Jakobsson P., et al., 2005, *ApJ*, 629, 45
Jakobsson P., et al., 2006, *A&A*, 447, 897
Jakobsson P., et al., 2012, *ApJ*, 752, 62
Japelj J., et al., 2015, *A&A*, 579, A74
Jones E., Oliphant T., Peterson P., 2001, *SciPy: Open source scientific tools for Python*, <http://www.scipy.org/>
Jones A., Noll S., Kausch W., Szyszka C., Kimeswenger S., 2013, *A&A*, 560, A91
Kann D. A., et al., 2017, eprint arXiv:1706.00601
Kausch W., et al., 2015, *A&A*, 576, A78
Krühler T., et al., 2011, *A&A*, 534, A108
Krühler T., et al., 2013, *A&A*, 557, A18
Krühler T., et al., 2015, *A&A*, 581, A125
Letchworth K. L., Benner D. C., 2007, *JQSRT*, 107, 173
Levan A. J., et al., 2013, *ApJ*, 781, 13
Levesque E. M., Kewley L. J., Graham J. F., Fruchter A. S., 2010, *ApJ*, 712, L26
Lien A., Sakamoto T., Gehrels N., Palmer D. M., Barthelmy S. D., Graziani C., Cannizzo J. K., 2014, *ApJ*, 783, 24
Lien A., et al., 2016, *ApJ*, 829, 7
López S., et al., 2016, *A&A*, 594, A91
Lyons N., O'Brien P. T., Zhang B., Willingale R., Troja E., Starling R. L., 2010, *MNRAS*, 402, 705
Melandri A., et al., 2012, *MNRAS*, 421, 1265
Michałowski M. J., et al., 2016, pp 1–16
Micol A., Arnaboldi M., Delmotte N. A. R., Mascetti L., Retzlaff J., 2016, *International Society for Optics and Photonics*, p. 991030, doi:10.1117/12.2232655, <http://proceedings.spiedigitallibrary.org/proceeding.aspx?doi=10.1117/12.2232655>
Modigliani A., et al., 2010, *SPIE Astron. Telesc. + Instrum.*, 7737, 773728
Moffat A. F. J., 1969, *A&A*, 3, 455
Molinari E., et al., 2006, *A&A*, 469, 6
Noll S., Kausch W., Barden M., Jones A. M., Szyszka C., Kimeswenger S., Vinther J., 2012, *A&A*, 543, A92
Noterdaeme P., et al., 2012, *A&A*, 547, L1
Nysewander M., Fruchter A. S., Pe'er A., 2009, *ApJ*, 701, 824
Oesch P. A., et al., 2016, *ApJ*, 819, 129
Pagnini G., Mainardi F., 2010, *JCoAM*, 233, 1590
Perley D. A., et al., 2009, *AJ*, 138, 1690
Perley D. A., et al., 2013, *ApJ*, 778, 128
Perley D. A., et al., 2015, *ApJ*, 801, 102
Perley D. A., et al., 2016a, *ApJ*, 817, 7
Perley D. A., et al., 2016b, *ApJ*, 817, 8
Perley D. A., et al., 2016c, *ApJ*, 817, 8
Perley D. A., et al., 2017, *Mon. Not. R. Astron. Soc. Lett.*, 465, L89
Piran T., 2005, *RvMP*, 76, 1143
Planck Collaboration et al., 2016, *A&A*, 594, A13
Prochaska J. X., Chen H.-W., Dessauges-Zavadsky M., Bloom J. S., 2007, *ApJ*, 666, 267
Prochaska J. X., et al., 2009, *ApJ*, 691, L27
Ricker G. R., Team H. S., 2004, *Am. Astron. Soc. HEAD Meet. #8*, id.18.06; *Bull. Am. Astron. Soc. Vol. 36*, p.942, 36, 942
Rol E., Wijers R. A. M. J., Kouveliotou C., Kaper L., Kaneko Y., 2005, *ApJ*, 624, 868
Rossi A., et al., 2012, *A&A*, 545, A77
Salvaterra R., et al., 2009, *Nature*, 461, 1258
Salvaterra R., et al., 2012, *ApJ*, 749, 68

- Sánchez-Ramírez R., et al., 2017, *MNRAS*, 464, 4624
- Savaglio S., 2006, *NJPh*, 8, 195
- Schady P., et al., 2015, *A&A*, 579, A126
- Schlaflly E. F., Finkbeiner D. P., 2011, *ApJ*, 737, 103
- Schlegel D. J., Finkbeiner D. P., Davis M., 1998, *ApJ*, 500, 525
- Schulze S., Malesani D., Cucchiara A., Tanvir N. R., Krühler T., Postigo A. D. U., Leloudas G., 2014, *A&A*, 569, 1
- Selsing J., Fynbo J. P. U., Christensen L., Krogager J.-K., 2015, *A&A*, 579, 14
- Selsing J., et al., 2017, pp 1–8
- Smette A., et al., 2015, *A&A*, 576, A77
- Sparre M., et al., 2011, *ApJ*, 735, L24
- Sparre M., et al., 2014, *ApJ*, 785, 150
- Starling R. L. C., et al., 2011, *MNRAS*, 411, 2792
- Tanvir N. R., et al., 2009, *Nature*, 461, 1254
- Tanvir N. R., Levan A. J., Fruchter A. S., Hjorth J., Hounsell R. A., Wiersema K., Tunnicliffe R. L., 2013, *Nature*, 500, 547
- Tepper García T., 2006, *MNRAS*, 369, 2025
- Thone C. C., Greiner J., Savaglio S., Jehin E., 2007, *ApJ*, 671, 628
- Thöne C. C., et al., 2013, *MNRAS*, 428, 3590
- Trujillo I., Aguerri J. A. L., Cepa J., Gutiérrez C. M., 2001, *MNRAS*, 328, 977
- Turpin D., Heussaff V., Dezalay J.-P., Atteia J.-L., Klotz A., Dornic D., 2016, *ApJ*, 831, 28
- Vergani S. D., et al., 2011, *A&A*, 535, A127
- Vergani S. D., et al., 2015, *A&A*, 581, A102
- Vernet J., et al., 2009, *Proc. Int. Astron. Union*, 5, 535
- Vernet J., et al., 2011, *A&A*, 536, A105
- Vreeswijk P. M., et al., 2007, *A&A*, 468, 83
- Vreeswijk P. M., et al., 2013, *A&A*, 549, A22
- Wiersema K., et al., 2012, *MNRAS*, 426, 2
- Wijers R. A. M. J., Bloom J. S., Bagla J. S., Natarajan P., 1998, *MNRAS*, 294, L13
- de Ugarte Postigo A., et al., 2010, *A&A*, 513, A42
- van Dokkum P. G., 2001, *PASP*, 113, 1420
- van der Horst A. J., Kouveliotou C., Gehrels N., Rol E., Wijers R. A. M. J., Cannizzo J. K., Racusin J., Burrows D. N., 2009, *ApJ*, 699, 1087

Table 1: The full sample of afterglows or hosts observed in the program. We here list the burst names and details of the spectroscopic observations. The exposure times and slit widths are given in the order UVB/VIS/NIR. The column Δt shows the time after trigger when the spectroscopic observation was started. Mag_{acq} gives the approximate magnitude (typically in the R -band) of the afterglow in the acquisition image.

GRB	Obs Date	Exptime (ks)	Slit width (arcsec)	Airmass	Seeing (arcsec)	Δt (hr)	Mag_{acq}	Redshift	Ref
GRB090313 ^a	2009-03-15	6.9/6.9/6.9	1.0/0.9/0.9	1.2–1.4	1.5	45	21.6	3.3736	(1)
GRB090530 ^a	2009-05-30	4.8/4.8/4.8	1.0/1.2/1.2	1.6–2.2	1.7	20.6	22	1.266	(2)
GRB090809 ^a	2009-08-10	7.2/7.2/7.2	1.0/0.9/0.9	1.2–1.1	1.1	10.2	21	2.737	(2,3)
GRB090926 ^a	2009-09-27	7.2/7.2/7.2	1.0/0.9/0.9	1.4–1.5	0.7	22	17.9	2.1062	(4)
GRB091018	2009-10-18	2.4/2.4/2.4	1.0/0.9/0.9	2.1–1.8	1.0	3.5	19.1	0.9710	(5)
GRB091127	2009-12-02	6.0/6.0/6.0	1.0/0.9/0.9	1.1–1.2	1.0	101	21.2	0.490	(6)
GRB100205A	2010-02-08	10.8/10.8/10.8	1.0/0.9/0.9	1.9–1.8	0.9	71	>24	–	(2)
GRB100219A	2010-02-20	4.8/4.8/4.8	1.0/0.9/0.9	1.3–1.1	0.8	12.5	23	4.667	(7)
GRB100316B	2010-03-16	2.4/2.4/2.4	1.0/0.9/0.9	2.0–2.4	0.6	0.7	18.2	1.18	(2)
GRB100316D-1 ^b	2010-03-17	3.6/3.6/3.6	1.0/0.9/0.9	1.2–1.3	0.8	10	21.5	0.059	(8)
GRB100316D-2	2010-03-19	2.4/2.4/2.4	1.0/0.9/0.9	1.1–1.2	0.9	58	20.2	0.059	(8)
GRB100316D-3	2010-03-20	2.6/2.6/3.2	1.0/0.9/0.9	1.1–1.2	1.1	79	19.9	0.059	(8)
GRB100316D-4	2010-03-21	2.6/2.6/3.2	1.0/0.9/0.9	1.1–1.2	1.5	101	19.9	0.059	(8)
GRB100418A-1	2010-04-19	4.8/4.8/4.8	1.0/0.9/0.9	1.6–1.3	0.7	8.4	18.1	0.624	(9)
GRB100418A-2	2010-04-20	4.8/4.8/4.8	1.0/0.9/0.9	1.2–1.3	0.6	34	19.2	0.624	(9)
GRB100418A-3	2010-04-21	4.8/4.8/4.8	1.0/0.9/0.9	1.2–1.4	0.7	58	>24	0.624	(9)
GRB100424A ^c	2013-03-11	4.8/4.8/4.8	1.0/0.9/0.9	1.1–1.2	0.9	25239.1	>24	2.465	(2)
GRB100425A	2010-04-25	2.4/2.4/2.4	1.0/0.9/0.9	1.5–1.3	0.7	4	20.6	1.755	(2,3)
GRB100615A ^c	2013-03-05	4.8/4.8/4.8	1.0/0.9/0.9	1.0–1.1	0.9	23858.8	>24	1.398	(2)
GRB100621A	2010-06-21	2.4/2.4/2.4	1.0/0.9/0.9	1.3–1.4	1.0	7.1		0.542	(2)
GRB100625A ^{c,f}	2010-07-07	4.8/4.8/4.8	1.0/0.9/0.9	1.1–1.0	0.8	278.7	>24	0.452	(2)
GRB100724A ^{a,d}	2010-07-24	4.2/4.2/4.2	1.0/0.9/0.9	1.5–2.3	0.7	0.2		1.288	(2)
GRB100728B ^e	2010-07-29	7.2/7.2/7.2	1.0/0.9/0.9	1.5–1.1	0.6	22	23	2.106	(2)
GRB100814A-1 ^d	2010-08-14	0.9/0.9/0.9	1.0/0.9/0.9	1.9–1.7	0.5	0.9	19	1.439	(2)
GRB100814A-2	2010-08-14	4.8/4.8/4.8	1.0/0.9/0.9	1.5–1.2	0.7	2.1	19	1.439	(2)
GRB100814A-3	2010-08-18	4.8/4.8/4.8	1.0/0.9/0.9	1.2–1.0	0.6	98	20	1.439	(2)
GRB100816A ^f	2010-08-17	4.8/4.8/4.8	1.0/0.9/0.9	1.8–1.6	0.8	28.4		0.805	(2)
GRB100901A	2010-09-04	2.4/2.4/2.4	1.0/0.9/0.9	1.5–1.5	1.9	66	>24	1.408	(10)
GRB101219A	2010-12-19	7.2/7.2/7.2	1.0/0.9/0.9	1.1–1.7	1.8	3.7		0.718	(2)
GRB101219B-1 ^a	2010-12-20	4.8/4.8/4.8	1.0/0.9/0.9	1.6–2.6	1.4	11.6	20	0.552	(11)
GRB101219B-2 ^a	2011-01-05	7.2/7.2/7.2	1.0/0.9/0.9	1.2–2.0	1.0	394	22.7	0.552	(11)
GRB101219B-3 ^a	2011-01-25	7.2/7.2/7.2	1.0/0.9/0.9	1.4–2.1	0.7	886	>24	0.552	(11)
GRB110128A	2011-01-28	7.2/7.2/7.2	1.0/0.9/0.9	2.0–1.6	0.6	5.5	22.5	2.339	(2)
GRB110407A	2011-04-08	9.6/9.6/9.6	1.0/0.9/0.9	1.4–1.3	2.1	12.4	23	–	(2)
GRB110709B ^c	2013-03-19	7.2/7.2/7.2	1.0/0.9/0.9	1.6–1.1	0.9	14834.8	>24	2.109	(2)
GRB110715A ^a	2011-07-16	0.6/0.6/0.6	1.0/0.9/0.9	1.1–1.1	1.6	12.3	18.5	0.823	(2)
GRB110721A ^a	2011-07-22	2.4/2.4/2.4	1.0/0.9/0.9	1.2–1.4	2.3	28.7	>24	0.382	(2)
GRB110808A	2011-08-08	2.4/2.4/2.4	1.0/0.9/0.9	1.2–1.1	1.0	3.0	21.2	1.3488	(2)
GRB110818A	2011-08-19	4.8/4.8/4.8	1.0/0.9/0.9	1.3–1.3	0.9	6.2	22.3	3.36	(2)
GRB111005A ^{a,c}	2013-04-01	1.2/1.2/1.2	1.0/0.9/0.9	1.3–1.3	0.7	13052.0	>24	0.013?	(2)
GRB111008A-1	2011-10-09	8.8/8.8/8.4	1.0/0.9/0.9	1.1–1.0	1.3	8.5	21	4.9898	(12)
GRB111008A-2	2011-10-10	8.0/8.0/7.2	1.0/0.9/0.9	1.3–1.0	0.9	20.1	22	4.9898	(12)
GRB111107A	2011-11-07	4.8/4.8/4.8	1.0/0.9/0.9	1.8–1.5	0.8	5.3	21.5	2.893	(2)
GRB111117A ^f	2011-11-19	4.8/4.8/4.8	1.0/0.9/0.9	1.5–1.4	0.7	38	>24	1.3?	(2)
GRB111123A-1	2011-11-24	6.2/6.6/6.6	1.0/0.9/0.9	1.6–1.1	0.8	12.2	>24	3.1516	(2)
GRB111123A-2 ^c	2013-03-07	2.4/2.4/2.4	1.0/0.9/0.9	1.0–1.0	0.5	11266.1	>24	3.1516	(2)
GRB111129A	2011-11-30	3.6/3.6/3.6	1.0/0.9/0.9	1.6–2.1	1.9	8.7	>24	1.080	(2)
GRB111209A-1	2011-12-10	4.8/4.8/4.8	1.0/0.9/0.9	1.1–1.2	0.8	17.7	20.1	0.677	(13)
GRB111209A-2	2011-12-29	9.6/9.6/9.6	1.0/0.9/0.9	1.2–2.0	1.0	497	23	0.677	(13)
GRB111211A ^a	2011-12-13	2.4/2.4/2.4	1.0/0.9/0.9	1.4–1.6	0.6	31	19.5	0.478	(2)
GRB111228A	2011-12-29	2.4/2.4/2.4	1.0/0.9/0.9	1.4–1.4	0.7	15.9	20.1	0.716	(2)
GRB120118B ^c	2013-02-13	3.6/3.6/3.6	1.0/0.9/0.9	1.1–1.0	0.7	9393.4	>24	2.943	(2)
GRB120119A-1	2012-01-19	2.4/2.4/2.4	1.0/0.9/0.9	1.1–1.1	0.6	1.4	17	1.728	(2)
GRB120119A-2	2012-01-19	1.2/1.2/1.2	1.0/0.9/0.9	1.8–1.9	0.5	4.5	20	1.728	(2)
GRB120119A-3 ^c	2013-02-26	4.8/4.8/4.8	1.0/0.9/0.6JH	1.0–1.1	1.8	9693.9	>24	1.728	(2)
GRB120211A-1 ^c	2013-02-17	4.8/4.8/4.8	1.0/0.9/0.9	1.1–1.4	1.3	8918.7	>24	2.346	(2)

Table 1: The full sample of afterglows or hosts observed in the program (continued).

GRB	Obs Date	Exptime	Slit width	Airmass	Seeing	Δt	Mag _{acq}	Redshift	Ref
		(ks)	(arcsec)		(arcsec)	(hr)			
GRB120211A-2 ^c	2013-03-20	3.6/3.6/3.6	1.0/0.9/0.9	1.1–1.2	1.2	9660.3	>24	2.346	(2)
GRB120224A	2012-02-25	2.4/2.4/2.4	1.0/0.9/0.9	1.7–2.1	1.3	19.8	22.3	1.10	(2)
GRB120311A ^a	2012-03-11	2.4/2.4/2.4	1.0/0.9/0.9	1.6–1.4	0.7	3.7	21.6	0.350	(2)
GRB120327A-1 ^a	2012-03-27	2.4/2.4/2.4	1.0/0.9/0.9	1.6–1.4	0.6	2.1	18.8	2.815	(14)
GRB120327A-2 ^a	2012-03-28	4.2/4.2/4.2	1.0/0.9/0.9	1.0–1.1	0.6	29	22.5	2.815	(14)
GRB120404A	2012-04-05	9.6/9.6/9.6	1.0/0.9/0.9JH	1.7–1.3	1.3	15.7	21.3	2.876	(2)
GRB120422A	2012-04-22	4.8/4.8/4.8	1.0/0.9/0.9	1.3–1.3	0.7	16.5	22	0.283	(15)
GRB120712A	2012-07-13	4.8/4.8/4.8	1.0/0.9/0.9	1.5–2.5	1.5	10.4	21.5	4.175	(2)
GRB120714B	2012-07-15	4.8/4.8/4.8	1.0/0.9/0.9JH	1.5–1.2	1.2	7.8	22.1	0.398	(2)
GRB120716A ^a	2012-07-19	3.6/3.6/3.6	1.0/0.9/0.9JH	1.8–2.6	1.1	62	20.9	2.486	(2)
GRB120722A ^b	2012-07-22	4.8/4.8/4.8	1.0/0.9/0.9	1.3–1.3	1.2	10.3	23.6	0.959	(2)
GRB120805A ^b	2012-08-14	3.6/3.6/3.6	1.0/0.9/0.9JH	1.3–1.7	0.9	218	>24	2.8?	(2)
GRB120815A ^a	2012-08-15	2.4/2.4/2.4	1.0/0.9/0.9	1.3–1.4	0.7	1.69	18.9	2.358	(16)
GRB120909A ^d	2012-09-09	1.2/1.2/1.2	1.0/0.9/0.9	1.6–1.6	1.6	1.7	21	3.929	(2)
GRB120923A	2012-09-23	9.6/9.6/9.6	1.0/0.9/0.9JH	1.2–1.4	1.0	18.5	>24	≥ 8	(2)
GRB121024A	2012-10-24	2.4/2.4/2.4	1.0/0.9/0.9	1.2–1.1	0.6	1.8	20	2.300	(17)
GRB121027A	2012-10-30	8.4/8.4/8.4	1.0/0.9/0.9	1.3–1.3	1.3	69.4	21.15	1.773	(2)
GRB121201A	2012-12-02	4.8/4.8/4.8	1.0/0.9/0.9JH	1.1–1.1	1.1	12.9	23	3.385	(2)
GRB121229A	2012-12-29	4.8/4.8/4.8	1.0/0.9/0.9JH	1.4–1.2	1.5	2	21.5	2.707	(2)
GRB130131B ^c	2013-03-09	7.2/7.2/7.2	1.0/0.9/0.9JH	1.3–1.6	1.1	874.1	>24	2.539	(2)
GRB130408A ^a	2013-04-08	1.2/1.2/1.2	1.0/0.9/0.9	1.0–1.0	0.9	1.9	20	3.758	(2)
GRB130418A	2013-04-18	1.2/1.2/1.2	1.0/0.9/0.9	1.4–1.3	1.2	4.6	18.5	1.222	(2)
GRB130427A	2013-04-28	1.2/1.2/1.2	1.0/0.9/0.9JH	1.8–1.8	0.8	16.5	19	0.340	(18)
GRB130427B	2013-04-28	1.2/1.2/1.2	1.0/0.9/0.9JH	1.2–1.0	1.0	20.3	22.7	2.780	(2)
GRB130603B ^f	2013-06-04	2.4/2.4/2.4	1.0/0.9/0.9	1.4–1.4	1.1	8.2	21.5	0.356	(19)
GRB130606A	2013-06-07	4.2/4.2/4.2	1.0/0.9/0.9JH	1.7–1.9	0.9	7.1	19	5.91	(20)
GRB130612A	2013-06-12	1.2/1.2/1.2	1.0/0.9/0.9	1.3–1.3	1.5	1.1	21.5	2.006	(2)
GRB130615A	2013-06-15	1.2/1.2/1.2	1.0/0.9/0.9	2.1–2.2	1.0	0.8	21	~ 3	(2)
GRB130701A	2013-07-01	1.2/1.2/1.2	1.0/0.9/0.9JH	2.0–2.0	1.4	5.5	19.9	1.155	(2)
GRB130925A	2013-09-25	5.88/6.0/6.9	1.0/0.9/0.9JH	1.0–1.0	0.6	3.5		0.347	(2)
GRB131011A ^a	2013-10-13	4.5/4.5/4.5	1.0/0.9/0.9	1.1–1.1	0.8	34.2	>24	1.874	(2)
GRB131030A	2013-10-31	3.6/3.6/3.6	1.0/0.9/0.9	1.1–1.1	1.1	3.4	18.0	1.296	(2)
GRB131103A	2013-11-05	2.4/2.4/2.4	1.0/0.9/0.9JH	1.1–1.1	1.0	5.8	20.48	0.599	(2)
GRB131105A	2013-11-05	4.8/4.8/4.8	1.0/0.9/0.9	1.3–1.4	0.8	1.3	22.4	1.686	(2)
GRB131117A	2013-11-17	4.8/4.8/4.8	1.0/0.9/0.9JH	1.3–1.2	1.7	1.1	20	4.042	(2)
GRB131231A ^a	2014-01-01	2.4/2.4/2.4	1.0/0.9/0.9JH	1.4–1.3	0.9	20.2	18.5	0.642	(2)
GRB140114A ^c	2014-03-28	5.4/5.4/5.4	1.0/0.9/0.9JH	1.7–1.7	1.2	1745.7	>24	2.8	(2)
GRB140213A ^a	2014-02-14	1.2/1.2/1.2	1.0/0.9/0.9JH	1.5–1.5	0.7	5.8	19.5	1.208	(2)
GRB140301A	2014-03-02	7.2/7.2/7.2	1.0/0.9/0.9JH	1.1–1.1	0.9	9	23.1	1.416	(2)
GRB140311A ^a	2014-03-13	7.6/6.3/8.4	1.0/0.9/0.9JH	1.2–1.2	0.6	32.5	>24	4.95	(2)
GRB140430A ^a	2014-04-30	1.2/1.2/1.2	1.0/0.9/0.9	2.0–1.8	1.6	2.5	19	1.601	(2)
GRB140506A-1	2014-05-07	4.8/4.8/4.8	1.0/0.9/0.9	1.3–1.4	0.7	8.8	20.9	0.889	(2)
GRB140506A-2	2014-05-08	4.8/4.8/4.8	1.0/0.9/0.9	1.2–1.3	0.7	32.9	>24	0.889	(2)
GRB140515A	2014-05-16	4.8/4.8/4.8	1.0/0.9/0.9	1.3–1.3	1.4	15.5		6.32	(2)
GRB140614A	2014-06-14	2.4/2.4/2.4	1.0/0.9/0.9	1.8–1.8	0.7	3.8	21.5	4.233	(2)
GRB140622A	2014-06-22	1.2/1.2/1.2	1.0/0.9/0.9	1.4–1.3	1.0	0.8		0.959	(2)
GRB141028A ^a	2014-10-29	2.4/2.4/2.4	1.0/0.9/0.9	1.5–1.4	1.0	15.4	20	2.332	(2)
GRB141031A ^{a c}	2015-01-29	2.4/2.4/2.4	1.0/0.9/0.9	1.2–1.3	0.8	10911.8	>24		(2)
GRB141109A-1	2014-11-09	2.4/2.4/2.4	1.0/0.9/0.9JH	1.5–1.7	0.8	1.9	19.2	2.993	(2)
GRB141109A-2	2014-11-10	4.3/4.3/4.5	1.0/0.9/0.9JH	1.7–2.0	0.8	25.4		2.993	(2)
GRB150206A ^a	2015-02-07	2.4/2.4/2.4	1.0/0.9/0.9	2.1–1.9	0.8	10	21.9	2.087	(2)
GRB150301B	2015-03-02	3.6/3.6/3.6	1.0/0.9/0.9JH	1.2–1.2	1.1	5.1		1.5169	(2)
GRB150403A	2015-04-04	2.4/2.4/2.4	1.0/0.9/0.9	1.6–1.7	nan	10.8	19.1	2.06	(2)
GRB150423A ^{d f}	2015-04-23	4.8/4.8/4.8	1.0/0.9/0.9	2.7–2.4	1.4	0.4		1.394	(2)
GRB150428A	2015-04-28	2.4/2.4/2.4	1.0/0.9/0.9JH	1.6–1.5	0.8	3.7			(2)
GRB150514A ^a	2015-05-15	2.4/2.4/2.4	1.0/0.9/0.9	2.3–2.1	0.9	28.4	19.5	0.807	(2)
GRB150518A ^a	2015-05-20	2.4/2.4/2.4	1.0/0.9/0.9JH	1.3–1.3	1.7	30.7	>24	0.256	(2)
GRB150616A-1 ^a	2015-06-17	2.4/2.4/2.4	1.0/0.9/0.9	1.4–1.5	0.8	5.7		0.988	(2)
GRB150616A-2 ^{a c}	2015-09-12	2.4/2.4/2.4	1.0/0.9/0.9JH	1.2–1.1	1.2	2091.9		0.988	(2)

Table 1: The full sample of afterglows or hosts observed in the program (continued).

GRB	Obs Date	Exptime	Slit width	Airmass	Seeing	Δt	Mag _{acq}	Redshift	Ref
		(ks)	(arcsec)		(arcsec)	(hr)			
GRB150727A	2015-07-28	3.6/3.6/2.4	1.0/0.9/0.9JH	1.2–1.2	1.4	5.0		0.313	(2)
GRB150821A ^d	2015-08-21	2.4/2.4/2.4	1.0/0.9/0.9	2.0–1.8	1.3	0.2	16	0.755	(2)
GRB150910A	2015-09-11	1.8/1.8/1.8	1.0/0.9/0.9JH	1.9–1.9	1.3	20.1		1.359	(2)
GRB150915A	2015-09-16	4.8/4.8/4.8	1.0/0.9/0.9JH	1.1–1.1	1.6	3.3	23	1.968	(2)
GRB151021A ^d	2015-10-21	4.2/4.2/4.2	1.0/0.9/0.9	1.0–1.1	1.4	0.75	18.2	2.33	(2)
GRB151027B	2015-10-28	2.4/2.4/2.4	1.0/0.9/0.9JH	1.5–1.7	1.2	5	20.5	4.063	(2)
GRB151029A	2015-10-29	1.2/1.2/1.2	1.0/0.9/0.9JH	1.9–1.7	1.1	1	20	1.423	(2)
GRB151031A	2015-10-31	4.2/4.2/4.2	1.0/0.9/0.9	1.1–1.1	1.1	0.3	20.4	1.167	(2)
GRB160117B	2016-01-18	4.8/4.8/4.8	1.0/0.9/0.9JH	1.1–1.2	1.1	13.5	21	0.87	(2)
GRB160203A ^d	2016-02-03	6.6/6.6/6.6	1.0/0.9/0.9	1.0–1.8	1.0	0.3	18	3.52	(2)
GRB160228A ^c	2016-03-12	4.8/4.8/4.8	1.0/0.9/0.9JH	1.7–1.7	1.0	295.8	>24	1.64	(2)
GRB160303A ^f	2016-03-04	4.8/4.8/4.8	1.0/0.9/0.9JH	1.6–1.5	0.8	19.1			(2)
GRB160314A	2016-03-15	4.8/4.8/4.8	1.0/0.9/0.9JH	1.3–1.3	0.8	13.0		0.726	(2)
GRB160410A ^{df}	2016-04-10	1.8/1.8/1.8	1.0/0.9/0.9	2.5–2.3	0.5	0.15	20.3	1.717	(2)
GRB160425A	2016-04-26	4.8/4.8/4.8	1.0/0.9/0.9JH	1.3–1.3	0.5	7.2		0.555	(2)
GRB160625B ^a	2016-06-27	2.4/2.4/2.4	1.0/0.9/0.9JH	1.3–1.3	0.7	30	19.1	1.406	(2)
GRB160804A-1 ^a	2016-08-04	2.4/2.4/2.4	1.0/0.9/0.9JH	1.4–1.3	0.6	22.4	21.2	0.736	(2)
GRB160804A-2 ^{a c}	2016-08-27	3.6/3.6/3.6	1.0/0.9/0.9JH	1.9–1.8	0.6	574.4	>24	0.736	(2)
GRB161001A	2016-10-01	2.4/2.4/2.4	1.0/0.9/0.9JH	1.2–1.3	0.5	6.1		0.891	(2)
GRB161007A ^c	2016-10-14	2.4/2.4/2.4	1.0/0.9/0.9JH	1.6–1.6	0.7	323	>24		(2)
GRB161014A	2016-10-15	4.8/4.8/4.8	1.0/0.9/0.9JH	1.1–1.2	0.5	11.6	21.4	2.823	(2)
GRB161023A ^a	2016-10-24	1.2/1.2/1.2	1.0/0.9/0.9JH	1.2–1.2	0.9	3	17.5	2.710	(2)
GRB161117A	2016-11-17	2.4/2.4/2.4	1.0/0.9/0.9	1.8–1.6	2.6	0.73	19	1.549	(2)
GRB161219B	2016-12-21	2.4/2.4/2.4	1.0/0.9/0.9JH	1.1–1.1	0.9	35.7		0.1475	(2)

Notes. ^(a) Not part of the statistical sample ^(b) Spectrum dominated by light from the host galaxy ^(c) Spectrum of the host galaxy taken long after the burst ^(d) RRM observation ^(e) ADC malfunction during observation ^(f) Short burst

References. (1) [de Ugarte Postigo et al. \(2010\)](#); (2) This work ; (3) [Skuladottir \(2010\)](#); (4) [D’Elia et al. \(2010\)](#); (5) [Wiersema et al. \(2012\)](#); (6) [Vergani et al. \(2011\)](#); [Cobb et al. \(2010\)](#); (7) [Thöne et al. \(2013\)](#); (8) [Bufano et al. \(2012\)](#) ; (9) [De Ugarte Postigo et al. \(2011\)](#) ; (10) [Hartoog et al. \(2013\)](#); (11) [Sparre et al. \(2011\)](#); (12) [Sparre et al. \(2014\)](#); (13) [Levan et al. \(2013\)](#); (14) [D’Elia et al. \(2014\)](#); (15) [Schulze et al. \(2014\)](#); (16) [Krühler et al. \(2013\)](#); (17) [Friis et al. \(2015\)](#)

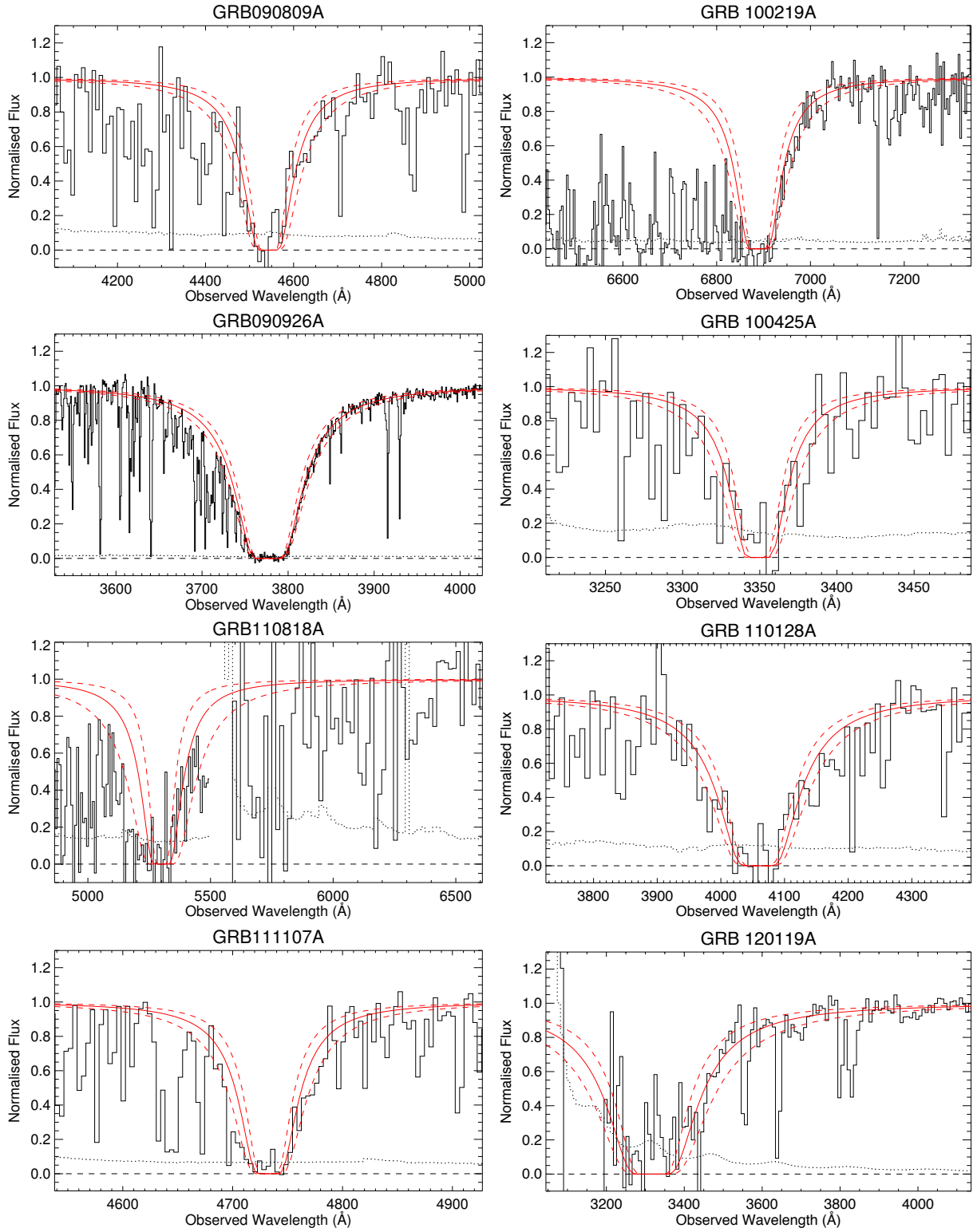


Fig. 10: Measurements of the hydrogen column-densities for all bursts with a clear Lyman alpha absorption system. In solid black is shown the spectrum with black dotted giving the corresponding 1- σ error. Black dashed shows zero flux density. The solid red line is the absorption of column density equal to the value presented in Tab. 3 with the 1- σ interval shown with dashed lines.

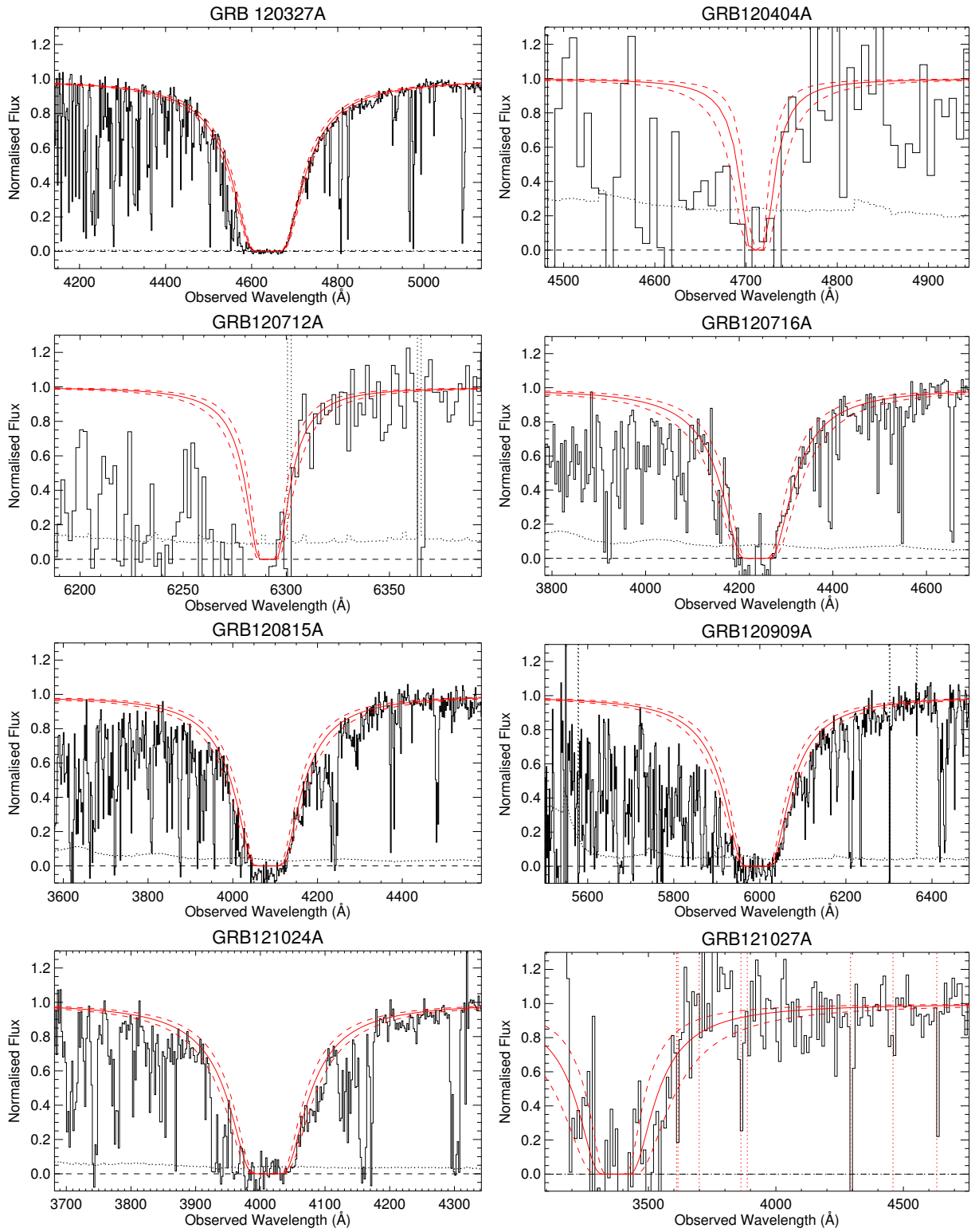


Fig. 10. continued.

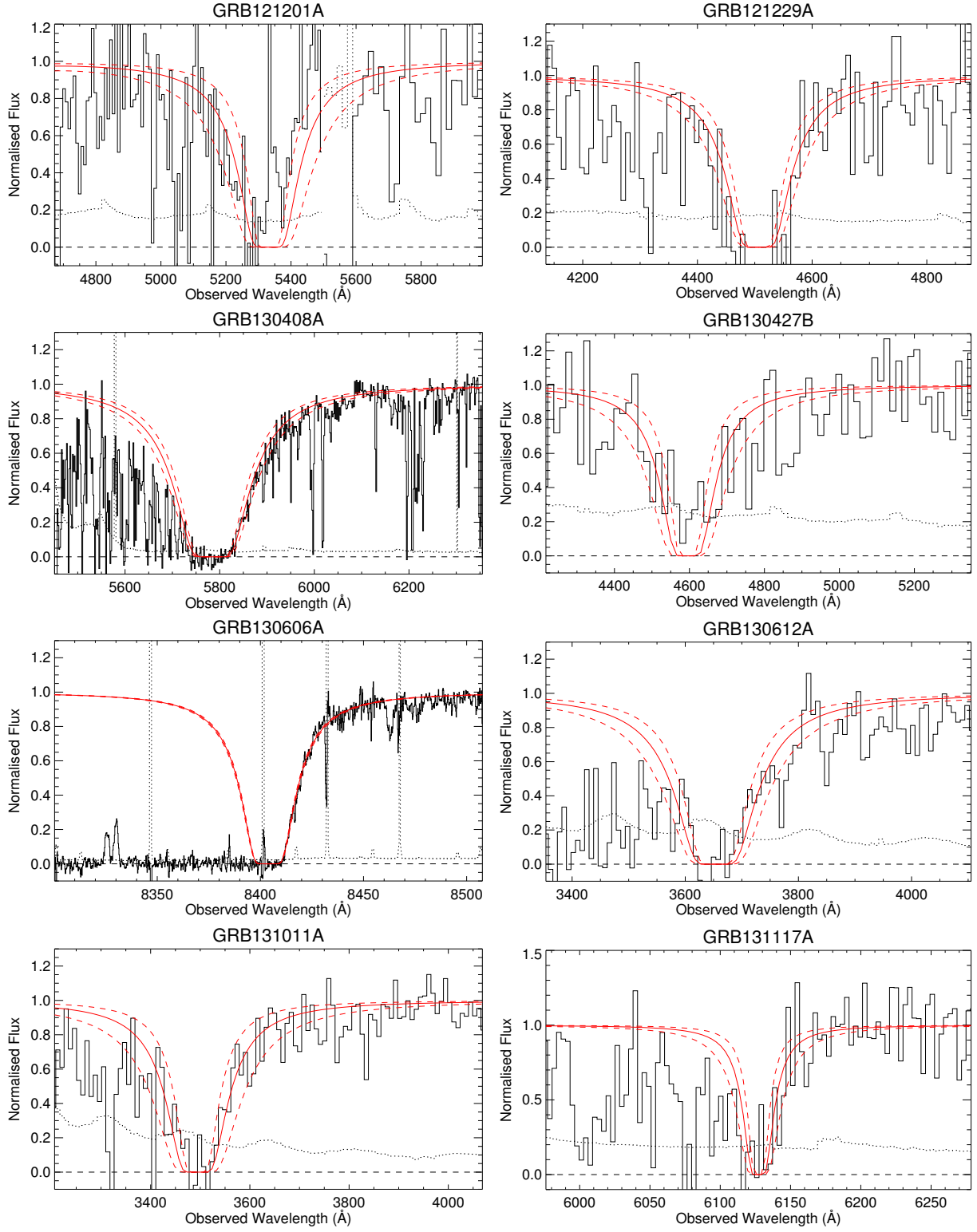


Fig. 10. continued.

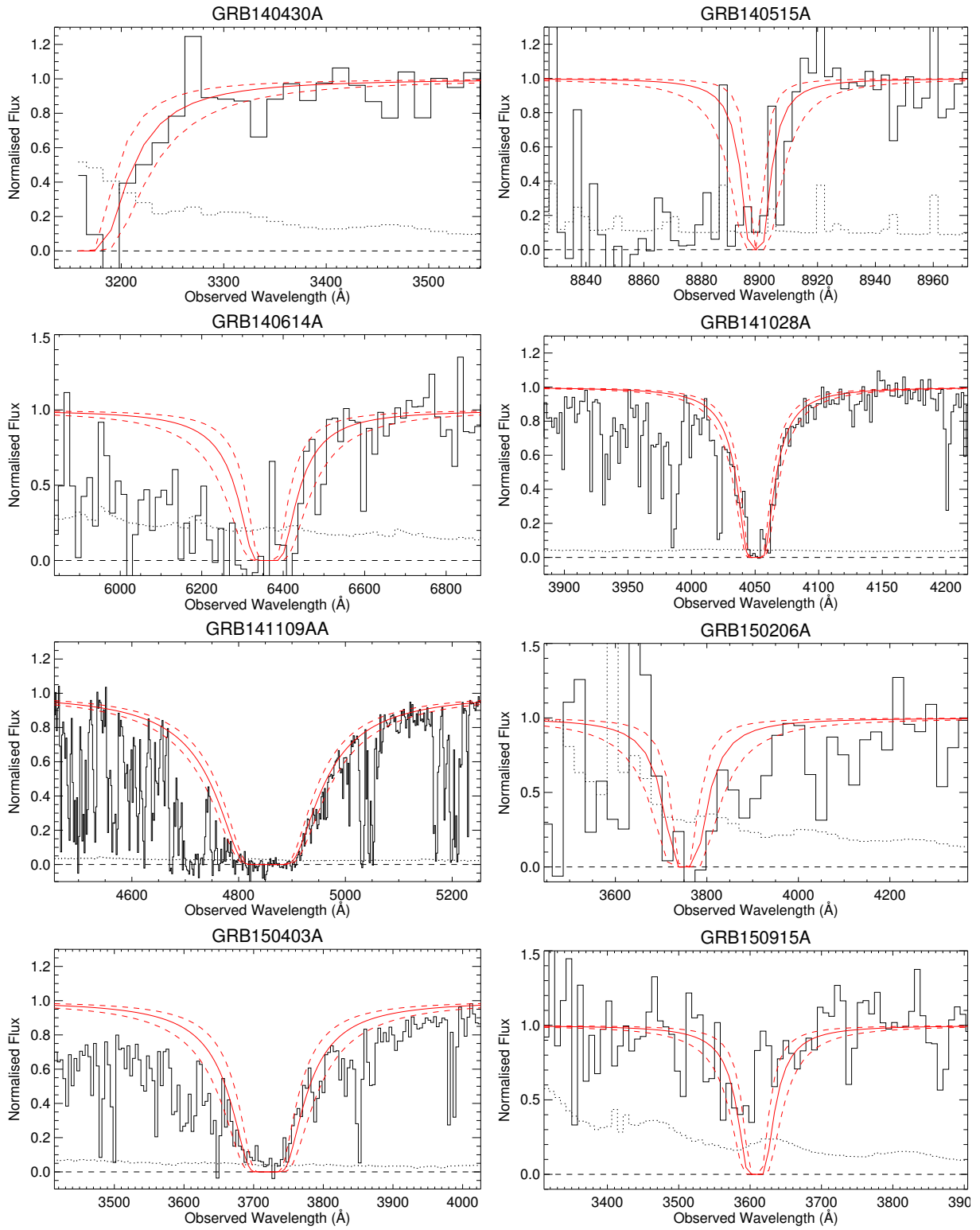


Fig. 10. continued.

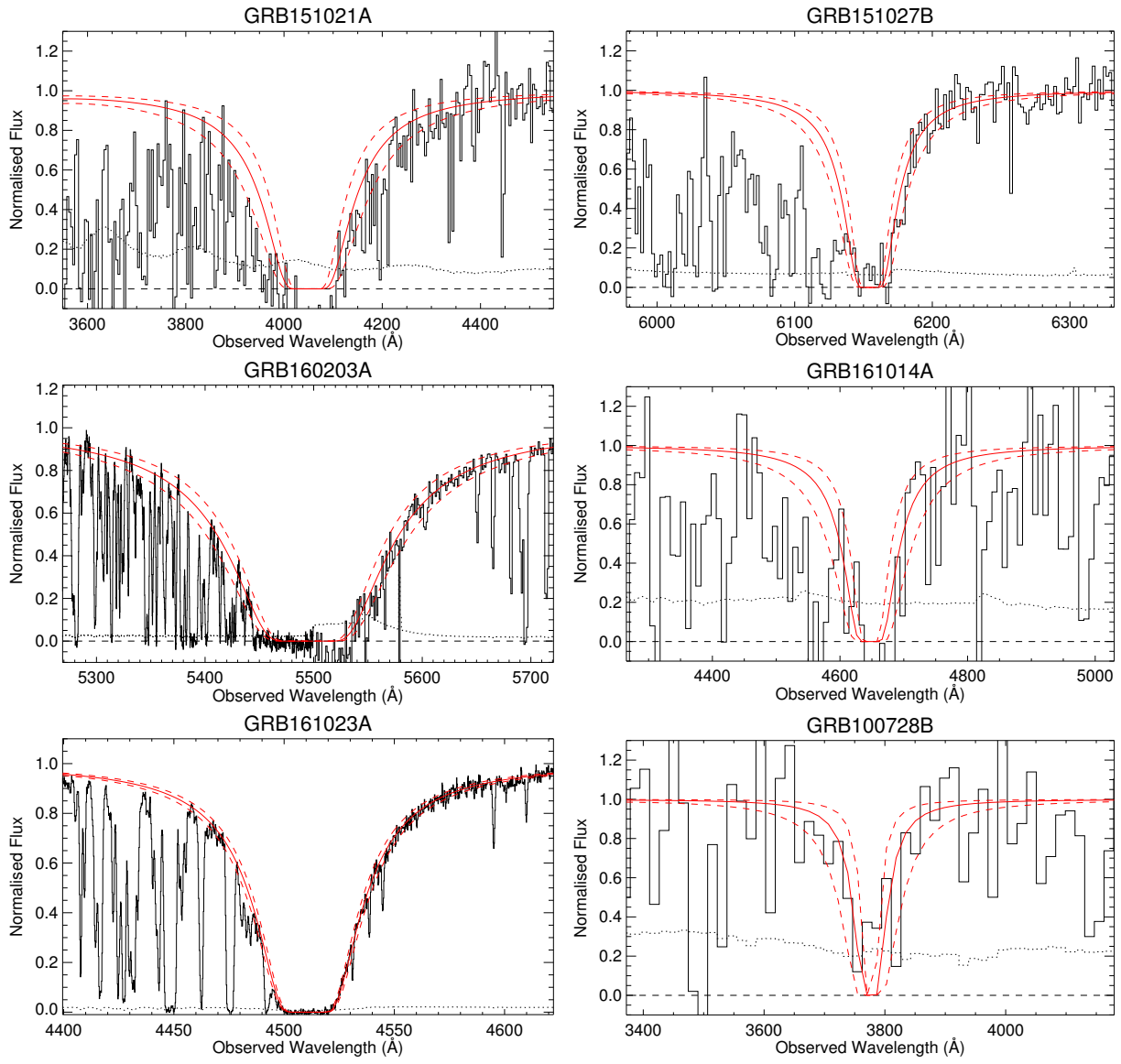


Fig. 10. continued.

Appendix A: The complex error function and the Voigt profile

When modeling the spectral PSF, we need to evaluate the Voigt-profile. The Voigt profile, which is the convolution of the Gaussian and Lorentzian profiles, can, centered at zero, be written as (Pagnini & Mainardi 2010)

$$\begin{aligned} V(\lambda, \sigma, \gamma) &= G(\lambda, \sigma) \otimes L(\lambda, \gamma) \\ &= \int_{-\infty}^{\infty} G(\xi, \sigma) L(\lambda - \xi, \gamma) d\xi \\ &= \int_{-\infty}^{\infty} \frac{1}{\sqrt{2\pi}\sigma} e^{-\left(\frac{\xi}{\sqrt{2}\sigma}\right)^2} \frac{1}{\gamma\pi} \frac{\gamma^2}{(\lambda - \xi)^2 + \gamma^2} d\xi \\ &= \frac{\gamma}{\sqrt{2}\sigma} \frac{1}{\pi^{3/2}} \int_{-\infty}^{\infty} \frac{e^{-\left(\frac{\xi}{\sqrt{2}\sigma}\right)^2}}{(\lambda - \xi)^2 + \gamma^2} d\xi. \end{aligned} \quad (\text{A.1})$$

We can by making the following substitution, $\xi = \sqrt{2}\sigma t$ and $d\xi = \sqrt{2}\sigma dt$, write it as

$$\begin{aligned} V(\lambda, \sigma, \gamma) &= \frac{\sqrt{2}\sigma}{\sqrt{\pi}} \frac{\gamma}{\pi} \int_{-\infty}^{\infty} \frac{e^{-t^2}}{(\lambda - \sqrt{2}\sigma t)^2 + \gamma^2} dt \\ &= \frac{1}{\sqrt{2\pi}\sigma} \frac{\gamma}{\pi} \int_{-\infty}^{\infty} \frac{e^{-t^2}}{\left(\frac{\lambda}{\sqrt{2}\sigma} - t\right)^2 + \left(\frac{\gamma}{\sqrt{2}\sigma}\right)^2} dt. \end{aligned} \quad (\text{A.2})$$

This form of the convolution is closely related to the complex probability function (Letchworth & Benner 2007; Abrarov & Quine 2015a),

$$W(z) = \frac{i}{\pi} \int_{-\infty}^{\infty} \frac{e^{-t^2}}{z - t} dt \quad (\text{A.3})$$

for any complex argument, $z = x + iy$. The complex probability function can be expressed as a sum of a real and imaginary part (Benner et al. 1995; Abrarov & Quine 2015b),

$$\begin{aligned} W(x, y) &= K(x, y) + iL(x, y) \\ &= \frac{y}{\pi} \int_{-\infty}^{\infty} \frac{e^{-t^2}}{(x - t)^2 + y^2} dt + \frac{i}{\pi} \int_{-\infty}^{\infty} \frac{(x - t)e^{-t^2}}{(x - t)^2 + y^2} dt, \end{aligned} \quad (\text{A.4})$$

where is the real part, $\text{Re}[W(x, y)] = \sqrt{2\pi}\sigma V(\lambda, \sigma, \gamma)$ if $x = \frac{\lambda}{\sqrt{2}\sigma}$ and $y = \frac{\gamma}{\sqrt{2}\sigma}$, which can be obtained by using the complex argument, $z = \frac{\lambda + iy}{\sqrt{2}\sigma}$, in the complex probability function. If $\text{Im}[z] \geq 0$, which is always guaranteed for the width of a spectral profile, the complex probability function equals the complex error function. The complex error function has numerous, fast, numerical approximations where in this work we use the `scipy.special.wofz` (Jones et al. 2001) implementation.

Appendix B: Notes on Individual objects

Appendix B.1: GRB 090313 ($z = 3.373$)

The first GRB ever observed with X-shooter, during the commissioning of the instrument, this data formed the basis of GCN #9015¹¹ and is published in de Ugarte Postigo et al. (2010).

¹¹ <http://gcn.gsfc.nasa.gov/gcn3/9015.gcn3>

Due to the lingering brightness of GRB 090313, 6.9 ks spectroscopic integration starting 45 hours after the BAT trigger reveals a wealth of absorption features superposed on the afterglow continuum at a common redshift of $z = 3.373$. Two intervening systems at $z = 1.959$ and $z = 1.800$ are identified based on strong Mg II-absorption. Because this burst is observed before the instrument is science-verified, it does not enter into the statistical sample.

Appendix B.2: GRB 090530 ($z = 1.266$)

Observed during paranalization of the instrument, this data forms the basis of GCN #15571¹², but is not published elsewhere. Observations began 20.6 hours after the BAT trigger and 4.8 ks spectroscopic integration in all three arms reveals the absorption signature for a host at $z = 1.266$ from the detection of Mg II, Mg I, Si II, Fe II, Al III. Because this burst is observed before the instrument is science-verified, it does not enter into the statistical sample.

Appendix B.3: GRB 090809 ($z = 2.737$)

Observed during the first science verification period and was used for GCN #9761¹³ and is additionally used as the basis for the master thesis by Ása Skúladóttir (2010). 7.2 ks integration starting 10.2 hours after the GRB trigger notice yields the clear afterglow continuum in all arms from with Lyman Limit located in the beginning of the UVB coverage. The simultaneous detection of absorption lines identified as Ly α , Si II, [O I], Si I*, Si IV, C IV, Fe II, Al II, Al III and Mg II at $z = 2.737$ sets it as the redshift of the GRB. Because this burst is observed before the instrument is science-verified, it does not enter into the statistical sample.

Appendix B.4: GRB 090926 ($z = 2.106$)

Starting during the second science verification period, this dataset forms the basis of GCN #9942¹⁴ and is additionally published in D'Elia et al. (2010). Spectroscopic integration started 22 hours after the BAT trigger and from the acquisition camera the optical afterglow has $R = 17.9$ mag (vega) at the beginning of the observations which causes a very continuum to be seen in all arms. An absorption trough due to Ly α is clearly visible along with numerous metal resonance lines C IV, Si II, Si I*, Fe II, Mg II, all at $z = 2.106$, marks this as the redshift of the GRB. Because this burst is observed before the instrument is science-verified, it does not enter into the statistical sample.

Appendix B.5: GRB 091018 ($z = 0.971$)

The first burst observed during normal operation after science verification was completed and there is the first burst that enter the statistical sample. This data is the basis for GCN # 10042¹⁵ and is published in Wiersema et al. (2012). With a bright afterglow and a rapid follow-up, this spectrum is of pristine quality. The afterglow continuum is bright throughout all spectroscopic arms which allows the ready detection of Al II, Al III, Fe II, Mn II, Mg II, Mg I, and Ca II located at $z = 0.971$, setting is as the redshift of the host.

¹² <http://gcn.gsfc.nasa.gov/gcn3/15571.gcn3>

¹³ <http://gcn.gsfc.nasa.gov/gcn3/9761.gcn3>

¹⁴ <http://gcn.gsfc.nasa.gov/gcn3/9942.gcn3>

¹⁵ <http://gcn.gsfc.nasa.gov/gcn3/10042.gcn3>

Appendix B.6: GRB 091127 ($z = 0.490$)

Obtained 4 days after the burst trigger, this data forms the basis for GCN # 10233¹⁶ and is published in Vergani et al. (2011). Due to the late follow-up and a nearby moon, the S/N of the afterglow continuum is poor especially in the UVB arm, why no clear absorption lines are detected against the afterglow continuum, although see Vergani et al. (2011) which report a tentative detection of Mg II. Emission lines from the underlying host is clearly visible with lines from [O II], H β , [O III], and H α all at $z = 0.490$. This bursts is additionally associated with SN2009nz.

Appendix B.7: GRB 100205A ($z = na$)

Observed 3 days after the *Swift* trigger. No afterglow or host detected in 10.8 ks. GRB likely located at high redshift¹⁷. The spectrum has not otherwise been published previously.

Appendix B.8: GRB 100219A ($z = 4.667$)

The data presented here also formed the basis of GCN # 10441¹⁸ and is published in Thöne et al. (2013). Observations started 12.5 hours after the *Swift* trigger and has a total exposure time of 4.8 ks. Absorption features, including those of Ly α and from a multitude of ions are detected against the afterglow continuum at $z = 4.667$. Additionally, absorption from an intervening system is found at $z = 2.181$.

Appendix B.9: GRB 100316B ($z = 1.180$)

The data presented here also formed the basis of GCN # 10495¹⁹. The spectrum has not otherwise been published previously. Observations started 44 minutes after the *Swift* trigger and has a total exposure time of 2.4 ks. Absorption features from Fe II, Al II, Al III, Mg II and Mg I are well detected against the afterglow continuum at $z = 1.180$. Additionally, strong absorption lines from Fe II and Mg II from an intervening system are found at $z = 1.063$.

Appendix B.10: GRB 100316D ($z = 0.059$)

The data presented here also formed the basis of GCN # 10512²⁰, GCN # 10513²¹, GCN # 10543²² and is published in Bufano et al. (2012) and Starling et al. (2011). This GRB is very close by and has an associated SN, SN2010bh, and has therefore undergone intense follow-up. The data presented here consists of a subset of the entire VLT/X-shooter campaign, covering the four first observing days while the afterglow still contributes significantly to the total emission. The first observations started 10 hours after the burst, before the SN was discovered, and targeted the star-forming 'A'-region (Starling et al. 2011), not the GRB. A very rich spectrum containing a multitude of emission lines puts the host at $z = 0.059$. For three consecutive nights, 58, 79 and 101 hours after the *Swift* trigger, the afterglow was observed as it transitioned into the spectrum of a high-velocity Ic-BL SN. The observations taken 79 and 101 hours after the burst are taken un-

der programme 084.D-0265(A) (PI: Benetti), but with an identical setup to the first two observations.

Appendix B.11: GRB 100418A ($z=0.624$)

The data presented here also formed the basis of GCN # 10620²³ and GCN # 10631²⁴ and is published in De Ugarte Postigo et al. (2011). The burst have been followed up in three epochs of observations, 0.4, 1.4, and 2.4 days after the burst, each lasting 4.8 ks. The unambiguous redshift of the host, $z = 0.624$, is found from the simultaneous detection of emission features belonging to nebular lines, including H I, [O II], [O III], [Ne III], [N II], [S II], [S III], and [He I] as well as absorption features due to the presence of Zn II, Cr II, Fe II, Mn II, Mg II, Mg I, Ti II, and Ca II, all at a consistent redshift. Temporal evolution of the fine structure lines belonging to Fe II* is found between the epochs.

Appendix B.12: GRB 100424A ($z=2.465$)

The data presented here also formed the basis of GCN # 14291²⁵. The spectrum has not otherwise been published previously. Observations carried out, long after the burst has faded. Emission lines from the host are detected at $z = 2.465$.

Appendix B.13: GRB 100425A ($z=1.1755$)

The data presented here also formed the basis of GCN # 10684²⁶ and is used in Skuladottir (2010), but not published elsewhere. Observations started 4 hours after the *Swift* trigger, totaling 2.4 ks. Absorption features from Mg II and Fe II in the afterglow continuum are detected at $z = 1.1755$.

Appendix B.14: GRB 100615A ($z=1.398$)

The data presented here also formed the basis of GCN # 14264²⁷, but not published elsewhere. Host observation of a dark burst (D'Elia & Stratta 2011) taken long after the afterglow has faded. Emission lines from the host belonging to [O II], [Ne III], [O III] and H α are detected at a common redshift of $z = 1.398$.

Appendix B.15: GRB 100621A ($z=0.542$)

The data presented here also formed the basis of GCN # 10876²⁸, but not published elsewhere. Beginning 7.1 hours after the GRB, 2.4 ks observations reveal emission lines from [O II], H β and [O III] at a common redshift of $z = 0.542$ and a very weak afterglow continuum.

Appendix B.16: GRB 100625A ($z=0.452$)

The data presented here is of the candidate host galaxy, taken long after the burst has faded and have not previously been published. 4.8 ks of exposure reveals a weak continuum present in all arms, but an absence of emission lines. This could indicate that the host primarily contains a older stellar population. The redshift, $z = 0.452$, is taken from Fong et al. (2013).

¹⁶ <http://gcn.gsfc.nasa.gov/gcn3/10233.gcn3>

¹⁷ <http://gcn.gsfc.nasa.gov/gcn3/10399.gcn3>

¹⁸ <http://gcn.gsfc.nasa.gov/gcn3/10441.gcn3>

¹⁹ <http://gcn.gsfc.nasa.gov/gcn3/10495.gcn3>

²⁰ <http://gcn.gsfc.nasa.gov/gcn3/10512.gcn3>

²¹ <http://gcn.gsfc.nasa.gov/gcn3/10513.gcn3>

²² <http://gcn.gsfc.nasa.gov/gcn3/10543.gcn3>

²³ <http://gcn.gsfc.nasa.gov/gcn3/10620.gcn3>

²⁴ <http://gcn.gsfc.nasa.gov/gcn3/10631.gcn3>

²⁵ <http://gcn.gsfc.nasa.gov/gcn3/14291.gcn3>

²⁶ <http://gcn.gsfc.nasa.gov/gcn3/10684.gcn3>

²⁷ <http://gcn.gsfc.nasa.gov/gcn3/14264.gcn3>

²⁸ <http://gcn.gsfc.nasa.gov/gcn3/10876.gcn3>

Appendix B.17: GRB 100724A* ($z = 1.288$)

The data presented here also formed the basis of GCN # 10971²⁹. The spectrum has not otherwise been published previously. The observations were carried out in RRM starting 11 min after the GRB trigger. See section 2.3, for a description of the RRM scheme. Absorption lines from several ionic species are detected in the afterglow continuum at a common redshift of $z = 1.288$. This is not a part of the statistical sample.

Appendix B.18: GRB 100728B ($z=2.106$)

The data presented here also formed the basis of GCN # 11317³⁰. The spectrum has not otherwise been published previously. Starting 22 hours after the burst trigger, 7.2 ks of observations reveals a faint afterglow continuum with Ly α - and Mg II-absorption at $z = 2.106$. Due to a malfunctioning ADC, the sensitivity of X-shooter is depressed with respect to normal operations, resulting in a poorer throughput. Additionally, the position of the trace on the slit moves due to atmospheric differential refraction.

Appendix B.19: GRB 100814A ($z=1.439$)

The spectra presented here has not been published previously. The observations consists of three visits, the first beginning only 0.9 hours after the *Swift* trigger, the other two visits were 2.13 and 98.40 hours after the trigger, respectively. A bright afterglow continuum is present in all visits, allowing identification of absorption features belonging to a wide range of ions at $z = 1.439$. A complex velocity structure in the absorption features belonging to Mg II, shows several components, separated by as much as 500km/s, pointing to a likely merger scenario in the host.

Appendix B.20: GRB 100816A ($z=0.805$)

The data presented here also formed the basis of GCN # 11123³¹. The spectrum has not otherwise been published previously. This short GRB was observed 28.4 hours after the GRB trigger. 4 x 1200 s of exposure reveals two distinct sets of emission lines, spatially offset $\lesssim 1''$, very close in redshift space, $z = 0.8034$ and $z = 0.8049$, indicating either an interacting host or some complex velocity structure of the host. Faint underlying continua are present under both sets of lines.

Appendix B.21: GRB 100901A ($z=1.408$)

The data presented here has been published in Hartoog et al. (2013). Because of the unusual lingering brightness of this GRB, 2.4s of observations taken 65.98 hours after the GRB trigger still reveals an afterglow continuum visible across the entire spectral coverage of X-shooter. Absorption lines from a wide range ion put the redshift at $z = 1.408$, with intervening absorption systems at $z = 1.3147$ and $z = 1.3179$.

Appendix B.22: GRB 101219A ($z=0.718$)

This data has not been published before. Starting 3.7 hours after the GRB trigger, 7.2 ks of exposure time reveals a very faint continuum in the visual and near-infrared, only visible when heavily

binning the images. No redshift estimate is available from these observations. Late-time Gemini-North observations reveal emission lines from the host at $z = 0.718$ ³².

Appendix B.23: GRB 101219B ($z=0.552$)

The data presented here also formed the basis of GCN # 11579³³ and is published in Sparre et al. (2011). The first observation, taken 11.6 hours after the burst trigger and lasting 4.8ks, reveals absorption from Mg II and Mg I in the host located at $z = 0.552$ on a featureless continuum visible across the entire coverage of X-shooter. Subsequent observations taken 16 and 37 days after the trigger shows the fading spectral signature of a SN, SN2010ma.

Appendix B.24: GRB 110128A ($z=2.339$)

These observations forms the basis of GCN # 11607³⁴, but has not been published before. Spectroscopic integration started 6.55 hours after the *Swift* trigger and lasted for a total of 7.2ks. The afterglow continuum is detected across the entire spectral coverage at moderate S/N. Absorption lines in the continuum is detected from Ly α , [O I], C II, Si IV, C IV, Si II and Fe II, all at a common redshift of $z = 2.339$. From the broad Ly α trough, a hydrogen column density $\log(N_{\text{HI}}/\text{cm}^{-2}) = 22.6 \pm 0.2$ is derived. An intervening system at $z = 2.20$ is tentatively identified from an absorption feature, likely due to C IV.

Appendix B.25: GRB 110407A ($z=na$)

These observations have not been published before. Starting 12.36 hours after the BAT trigger, 4.8 ks spectroscopic integration yield a very faint trace down to $\sim 4300\text{\AA}$, only visible after binning heavily. This could indicate a redshift, $z \sim 2.5$, but no emission lines or absorption lines are immediately visible to support this.

Appendix B.26: GRB 110709B ($z=2.109$ (NEW!!!!))

This is a late-time observation (> 1 year) and has previously been used in Perley et al. (2016a). In this reduction of the 7.2 ks spectroscopic integration, the tentative detection of [O III] reported in Perley et al. (2016a) is confirmed along with low-significance detection of H α at the end of the spectral coverage, both at a consistent redshift, $z = 2.109$, securing it as the redshift of the GRB.

Appendix B.27: GRB 110715A ($z=0.823$)

These observation, starting 12.3 hours after the trigger, have been published in Sánchez-Ramírez et al. (2017) and additionally formed the basis of GCN # 12164³⁵. Only a single exposure of 600 s was obtained, before strong winds interrupted the observations. A red continuum is detected across all arms and a multitude of absorption lines are superposed on the afterglow continuum. We identify lines belonging to Al II, Al III, Zn II, Cr II, Fe II, Mg II, Mg I, Ca II, and Ca II, all at $z = 0.823$, marking it as the redshift of the GRB.

²⁹ <http://gcn.gsfc.nasa.gov/gcn3/10971.gcn3>

³⁰ <http://gcn.gsfc.nasa.gov/gcn3/11317.gcn3>

³¹ <http://gcn.gsfc.nasa.gov/gcn3/11123.gcn3>

³² <http://gcn.gsfc.nasa.gov/gcn3/11518.gcn3>

³³ <http://gcn.gsfc.nasa.gov/gcn3/11579.gcn3>

³⁴ <http://gcn.gsfc.nasa.gov/gcn3/11607.gcn3>

³⁵ <http://gcn.gsfc.nasa.gov/gcn3/12164.gcn3>

Appendix B.28: GRB 110721A ($z=0.382$)

This is a Fermi burst with a LAT detection and thus outside the statistical sample, but nonetheless followed up due to the extremely high peak energy (Axelsson et al. 2012). Starting 28.7 after the burst trigger, 2.4ks spectroscopic observation reveals after heavy binning, a wide, faint trace down to $\sim 5800 \text{ \AA}$, offset by $2.5''$ relative to the centering of the slit. No good redshift measurement can be inferred from this. We have adopted the redshift from GCN # 12193³⁶

Appendix B.29: GRB 110808A ($z=1.348$)

This spectrum has already formed the basis of GCN # 12258³⁷, but is not published otherwise. Starting 3 hours after the *Swift* trigger, a rich spectrum is obtained in 2.4ks spectroscopic integration. The GRB afterglow continuum is visible across all three spectroscopic arms of VLT/X-shooter with additionally, emission lines identified as [O II], [O III], H α all at $z = 1.348$. At the same redshift, we identify absorption lines superposed on the afterglow continuum from Mg II and Fe II.

Appendix B.30: GRB 110818A ($z=3.36$)

Starting 6.15 hours after the BAT trigger, spectroscopic integration for 4.8ks reveals a moderate S/N GRB afterglow continuum, down to $\sim 5000 \text{ \AA}$. The simultaneous detection of absorption features identified as Ly α , Si II, C IV, Al II, Ca H, Ca K, and Mg II, and emission from the [O III]-doublet, securely sets $z = 3.36$ as the redshift of the GRB. This data forms the basis of GCN # 12284³⁸, but is not published elsewhere.

Appendix B.31: GRB 111005A ($z=0.013$)

The data presented here has previously been published in Michałowski et al. (2016). 2.4ks spectroscopic integration of the host galaxy, obtained long after the burst had faded, contains bright emission lines filling the entire slit on top of a broad, underlying stellar continuum. We identify emission lines from [O II], H δ , H γ , H β , [O III], [N II], H β , [S II], Ar III, and [S II], all at $z = 0.013$. Significant velocity structure of the lines across the spatial direction of the slit indicates a large degree of coherent motion relative to the line-of-sight.

Appendix B.32: GRB 111008A ($z=4.989$)

This data formed the basis of GCN # 12431³⁹ and is additionally published in Sparre et al. (2014). Observations of this GRB afterglow was initiated 7.71 hours after the BAT trigger and had a duration of 8.4ks. A second observational epoch started 20.1 hours and lasted for 6.6ks. The GRB afterglow continuum is well detected down to $\sim 7600 \text{ \AA}$, with several strong absorption features imprinted. All at a common $z = 4.990$ Ly α is clearly detected and we additionally detect lines identified as Si II, Fe II, C IV, Mg II, Si II*, [S II]*, [O I]*. An intervening DLA systems is additionally detected at $z = 4.61$ as seen from Ly α and Mg II absorption.

Appendix B.33: GRB 111107A ($z=2.893$)

GCN # 12542⁴⁰ is based on this spectrum, but it is not published elsewhere. Spectroscopic integration started 5.26 hours after the *Swift* trigger and consists of $4 \times 1200 \text{ s}$ integration in the UVB and VIS and $16 \times 300 \text{ s}$ in NIR, the observations ending in twilight. The GRB afterglow continuum is well detected across the arms with absorption lines from Ly α , C IV, Fe II, and Mg II, all at a consistent redshift of $z = 2.893$. Additionally an intervening Mg II system is detected at $z = 1.998$. From the Ly α absorption trough, we additionally infer $\log(N_{\text{HI}}/\text{cm}^{-2}) = 21.0 \pm 0.2$.

Appendix B.34: GRB 111117A ($z=2.211$)

This data has previously been used to form some of the basis of Selsing et al. (2017). Starting 37.3 hours after the BAT trigger, 4.8ks of spectroscopic integration yields faint emission lines identified at [O II], H β , [O III] and H α , all at a common $z = 2.211$, marking it as the redshift of the GRB. No afterglow continuum is detected.

Appendix B.35: GRB 111123A ($z=3.151$)

This data formed the basis of GCN # 14273⁴¹, but is not published elsewhere. Observed twice, the first time shortly after the GRB and the second long after the burst had faded, securely sets the redshift of the host at $z = 3.151$ based on the detection of emission lines identified as [O II] and [O III].

Appendix B.36: GRB 111129A ($z=1.080$)

Starting 8.26 hours after and lasting 3.6ks, these observations have previously been published in Krühler et al. (2015). A very faint continuum is visible after severe binning and a redshift is suggested in Krühler et al. (2015), based on the detection of [O II]. At this redshift, H β and [O II] are located in the gap between the VIS and NIR arm and H α is located in the middle of the *JH*-bandgap and there are therefore not detected.

Appendix B.37: GRB 111209A ($z=0.677$)

These spectra has previously been used in Levan et al. (2013); Greiner et al. (2015); Krühler et al. (2015); Kann et al. (2017) and additionally formed the basis for GCN # 12648⁴². The first epoch of spectroscopic observations was initiated 17.7 hours after the BAT trigger and lasted for 4.8 seconds. A very bright afterglow continuum is detected across the entire spectral coverage of X-shooter, with several absorption features imprinted. The absorption features are identified as Fe II, Mg II, Mg I, Ca H, and Ca K- all at a common redshift of $z = 0.677$. The second epoch, taken 20 days later, still contains a faint continuum detected across all arms. The detection of nebular emission lines identified as [O II], [O II] and H α at the same redshift, securely marks it at the redshift of this ultra-long GRB with accompanying GRB-SN.

³⁶ <http://gcn.gsfc.nasa.gov/gcn3/12193.gcn3>

³⁷ <http://gcn.gsfc.nasa.gov/gcn3/12258.gcn3>

³⁸ <http://gcn.gsfc.nasa.gov/gcn3/12284.gcn3>

³⁹ <http://gcn.gsfc.nasa.gov/gcn3/12431.gcn3>

⁴⁰ <http://gcn.gsfc.nasa.gov/gcn3/12542.gcn3>

⁴¹ <http://gcn.gsfc.nasa.gov/gcn3/14273.gcn3>

⁴² <http://gcn.gsfc.nasa.gov/gcn3/12648.gcn3>

Appendix B.38: GRB 111211A ($z=0.478$)

These data has formed the basis for GCN # 12677⁴³ and is also published in Krühler et al. (2015). Observations began 31 hours after the AGILE trigger and consisted of 4×600 s. A bright GRB afterglow continuum is detected across the entire spectral coverage of X-shooter with absorption and emission features visible. We identify absorption features due to Fe II, Mg II, and Ca II and emission lines from [O III] and H α , all at a common $z = 0.478$, which we suggest is the redshift of the GRB. Additionally detected in the GRB afterglow continuum is broad undulation, suggesting an accompanying SN.

Appendix B.39: GRB 111228A ($z=0.716$)

This data formed the basis of GCN # 12770⁴⁴ and is also published in Krühler et al. (2015). Observations began 15.9 hours after the BAT trigger and consist of 4×600 s. The GRB afterglow continuum is clearly detected in all the spectroscopic arms and superposed on the continuum are absorption features identified as due to Fe II, Mn II, Mg II, Mg I, Ca H, and Ca K, all at $z = 0.716$. Supporting this redshift measurement as the redshift of the GRB is the detection of nebular emission line from [O III].

Appendix B.40: GRB 120118B ($z = 2.943$)

The data presented here also formed the basis of GCN # 14225⁴⁵, but is not published otherwise. This late-time observation of the host of GRB 120118B consists of 3.6 ks exposures and contains emission lines belonging to [O II] and [O III] at $z = 2.943$, suggested to be redshift of the host.

Appendix B.41: GRB 120119A ($z = 1.728$)

The data presented here has been examined by Japelj et al. (2015) and ? who both find a significant amount of extinction, $A_V \approx 1$ mag. Three epochs of observations have been obtained, the first two immediately after the burst, and the last one long after the afterglow had faded. Starting 1.4 hours after the *Swift* trigger, the first epoch contains bright afterglow continuum. Rich in absorption features belonging to a multitude of ions at $z = 1.728$ is estimated for the host with intervening systems at $z = 1.476$, $z = 1.214$, $z = 0.662$ and $z = 0.632$. The second epoch, obtained 4.5 hours after the burst contains the fading afterglow. A third epoch is obtained > 1 year after the GRB in which emission lines from H β and H α are found at the redshift of the host, confirming the association of the absorption line system and the host. We also detect C I in absorption which indicates the presence of cold gas.

Appendix B.42: GRB 120211A ($z = 2.346$)

The data presented here has been published in Krühler et al. (2015). Two observations of the host of GRB 120211A has been obtained, starting 2013.02.17, > 1 year after the burst has faded. A redshift for this object has been reported by Krühler et al. (2015) and the features seen by those authors are reproduced in these reductions, confirming $z = 2.346$.

Appendix B.43: GRB 120224A ($z = 1.10$ NEW!!!)

The data presented here has formed the basis of GCN # 12991⁴⁶, and has also been published in Krühler et al. (2015). Starting 19.8 hours after the GRB trigger, a total exposure time of 2.4 ks reveals a faint continuum, starting at ~ 700 nm and extending all the way through 2500 nm. We detect a $\sim 2\sigma$ emission line which, if interpreted as H α , gives $z = 1.10$, supporting the redshift reported by Krühler et al. (2015).

Appendix B.44: GRB 120311 ($z = 0.350$ NEW!!!)

The data presented here has formed the basis of GCN # 12991⁴⁷, but is not published otherwise. Starting just before twilight, 3.65 hours after the burst, a faint afterglow continuum is detected at all wavelengths. Due to the faintness of the afterglow, no absorption features are discernible superposed on the continuum. Displaced from the afterglow continuum by $1''.4$, emission lines belonging to H β , [O III] and H α are detected at $z = 0.350$. The line belonging to H α shows some extended emission toward the afterglow continuum. The angular distance between the two sources correspond to a projected distance in the host plane of 6 kpc, posing a potential problem for the host redshift, unless the GRB occurred in a merging system. The extended emission in H α , supports this interpretation. This burst is not apart of the statistical sample.

Appendix B.45: GRB 120327A ($z = 2.813$)

The data presented here also formed the basis of GCN # 13134⁴⁸ and is published in D'Elia et al. (2014). The observation consists of two visits, 2.13 hrs and 29.98 hrs after the burst, with an afterglow continuum visible in all arms for both visits. We detect absorption features from Ly-limit, Ly α , C II/C III*, Si II/Si III*, Al I, Fe II and Mg II are detected at a consistent redshift, $z = 2.813$.

Appendix B.46: GRB 120404A ($z = 2.876$)

The data presented here has formed the basis of GCN # 13227⁴⁹, but is not published otherwise. 9.6 ks integration, starting 15.7 hours after the *Swift*-trigger reveals a low-intensity afterglow continuum on which absorption from Ly α is detected in two distinct regions at redshifts $z = 2.876$ and $z = 2.55$. These absorption systems are confirmed by ionic absorption features at both of these redshifts.

Appendix B.47: GRB 120422A ($z = 0.283$)

The data presented here also formed the basis of GCN # 13257⁵⁰ and is published in Schulze et al. (2014). A GRB-SN, this burst has been followed up multiple times. The data presented here only contain the first epoch in which the afterglow is still visible and before the rise of SN2012bz. Starting 16.5 hours after the burst, 4.8 ks integration time captures both the host and the burst in emission. A blue afterglow continuum is detected at all wavelengths covered by X-shooter, on which Mg II absorption at $z = 0.283$ is found. Offset by $1''.75$, the host is clearly detected at

⁴³ <http://gcn.gsfc.nasa.gov/gcn3/12677.gcn3>⁴⁴ <http://gcn.gsfc.nasa.gov/gcn3/12770.gcn3>⁴⁵ <http://gcn.gsfc.nasa.gov/gcn3/14225.gcn3>⁴⁶ <http://gcn.gsfc.nasa.gov/gcn3/12991.gcn3>⁴⁷ <http://gcn.gsfc.nasa.gov/gcn3/12991.gcn3>⁴⁸ <http://gcn.gsfc.nasa.gov/gcn3/13134.gcn3>⁴⁹ <http://gcn.gsfc.nasa.gov/gcn3/13227.gcn3>⁵⁰ <http://gcn.gsfc.nasa.gov/gcn3/13257.gcn3>

a consistent redshift with a rich emission line spectrum, the lines extending towards to burst.

Appendix B.48: GRB 120712A ($z = 4.175$)

The data presented here also formed the basis of GCN #13460⁵¹ and is not published elsewhere. 4.8 ks integration time, starting 10.5 hours after the BAT trigger, shows a bright afterglow continuum starting at ~ 472 nm, signifying the onset of the Lyman alpha forest, for a GRB located at $z = 4.175$. Absorption features from Ly α , Fe II, Mg II and Si II are readily detected at a consistent redshift.

Appendix B.49: GRB 120714B ($z = 0.398$)

The data presented here also formed the basis of GCN #13477⁵², but is not published elsewhere. Observations of this burst started 7.8 hours after the GRB trigger, lasting 4.8 ks. A continuum is visible across the entire spectral coverage of X-shooter, with both emission lines from [O II], H β , [O III] and H α , as well as absorption from Mg II detected at $z = 0.398$, securely setting it as the redshift of the GRB.

Appendix B.50: GRB 120716A ($z = 2.486$)

The data presented here also formed the basis of GCN #13494⁵³, but is not published elsewhere. Despite observations starting 62 hours after the *Swift* trigger and lasting 3.6 ks, a bright afterglow is clearly seen, along with a plethora of absorption features. Absorption of Ly α -photons in the host leaves a broad trough, from which the Lyman alpha forest is visible bluewards, all the way down to the Lyman limit. Metal absorption lines from C II, Si II, [O I], Fe II, C IV, Si IV, including fine structure transitions identified as C II*, Si II*, Fe II* and metastable [Ni II] lines are all detected at $z = 2.486$.

Appendix B.51: GRB 120722A ($z = 0.959$)

The data presented here also formed the basis of GCN #13507⁵⁴, but is not published elsewhere. On 4.8 ks integration time, starting 10 hours after the burst trigger, the simultaneous detection of absorption features belonging to Mg II and Fe II superposed on a blue continuum, and emission lines from [O II], H γ , H β , [O III] and H α , all at $z = 0.959$, confidently sets it as the redshift of the GRB.

Appendix B.52: GRB 120805A ($z \sim 3.9$ NEW!!!)

A separate reduction of this burst has been published in Krühler et al. (2015), but not otherwise. Starting 9 days after the burst trigger, this is host observation and does not contain any afterglow continuum. In 3.6 ks integration time, we detect a faint continuum visible from 450 nm and all the way through 2100 nm, in contrast to what is found previously. The continuum from 4500 - 600 nm is detected at very low significance. If the drop at 450 nm is the Lyman limit, this fits with Lyman alpha at ~ 600 nm, giving $z \sim 3.9$. The absence of nebular lines if due to [O II] falling in a telluric absorption band and the rest being shifted out of the wavelength coverage.

Appendix B.53: GRB 120815A* ($z = 2.358$)

Not a part of the statistical sample, this burst also formed the basis of GCN #13649⁵⁵ and is published in Krühler et al. (2013). Observations started 1.69 hours after the BAT trigger and consist of 2.4 ks integration. A bright afterglow continuum is detected across the entire spectral coverage of X-shooter, with a multitude of absorption lines superposed. Absorption features from the host at $z = 2.358$ include a DLA as well as metal absorption lines from [N V], [S II], Si II, [O I], C IV, Si IV, Fe II, Al II, Al III, Mn II, Mg II, and Mg I. Additionally fine structure lines from [Ni II] and Fe II are exited local to the GRB. Intervening systems are found at $z = 1.539$, $z = 1.693$, and $z = 2.00$.

Appendix B.54: GRB 120909A ($z = 3.929$)

The data presented here has formed the basis of GCN #13730⁵⁶, but is not published otherwise. A very rapid follow-up, starting only 1.7 hours after the BAT trigger, this 1.2 ks observation captures a very bright afterglow continuum, starting at 450 nm, signifying the onset of the Lyman limit for a system at $z = 3.929$. Absorption from high-column density hydrogen leaves very prominent absorption features in the form of Ly α , Ly β , and Ly γ , visible in the Lyman alpha forest. Metal absorption lines arising from Fe II, [Ni II], Si II, [S II], Al II, Al III, C II, [O I], C IV, and Zn II are all detected along with the corresponding fine structure lines from (Fe II*, Si II*, [O I]*, [O I]*, C II*), securely anchoring the redshift of the host.

Appendix B.55: GRB 120923A ($z \gtrsim 8?$)

Appendix B.56: GRB 121024A ($z = 2.300$)

The data presented here also formed the basis of GCN #13890⁵⁷ and is published in Friis et al. (2015). Also rapid, starting 1.8 hours after the *Swift* trigger, a bright afterglow continuum is visible across all arms. A broad absorption feature from Lyman alpha, along with narrow lines from C IV, Si II, Si IV, Fe II, [S II], and Al II, as well as fine structure lines associated with Si II* are all detected at $z = 2.300$, securely setting it as the redshift of the GRB.

Appendix B.57: GRB 121027A ($z = 1.773$)

The data presented here has formed the basis of GCN #13930⁵⁸, but is not published otherwise. Starting 69.6 hours after the GRB trigger, that we detect the afterglow continuum a so high significance in all arms with 8.4 ks integration, testifies to the brightness of this burst. The concurrent identification of emission lines from [O III] and absorption from C IV, Al II, Al III, Mg I, Mg II, and Fe II, tightly constrains the redshift of the burst to be ($z = 1.773$).

Appendix B.58: GRB 121201A ($z = 3.385$)

These data formed the basis for GCN #14035⁵⁹ and is additionally published in Krühler et al. (2015). These observations started 12.9 hours after the *Swift* trigger and consists of 4.8ks spectroscopic integration under good atmospheric conditions. The GRB afterglow continuum is well detected at all arms. A

⁵¹ <http://gcn.gsfc.nasa.gov/gcn3/13460.gcn3>

⁵² <http://gcn.gsfc.nasa.gov/gcn3/13477.gcn3>

⁵³ <http://gcn.gsfc.nasa.gov/gcn3/13494.gcn3>

⁵⁴ <http://gcn.gsfc.nasa.gov/gcn3/13507.gcn3>

⁵⁵ <http://gcn.gsfc.nasa.gov/gcn3/13649.gcn3>

⁵⁶ <http://gcn.gsfc.nasa.gov/gcn3/13730.gcn3>

⁵⁷ <http://gcn.gsfc.nasa.gov/gcn3/13890.gcn3>

⁵⁸ <http://gcn.gsfc.nasa.gov/gcn3/13930.gcn3>

⁵⁹ <http://gcn.gsfc.nasa.gov/gcn3/14035.gcn3>

broad absorption trough due to Ly α is visible at $z = 3.385$, which along with the detection of absorption features identified as Si IV, C IV, Al II, and Al III, marks it as the redshift of the GRB. In the middle of the Ly α trough, we additionally detect Ly α emission. By modelling the Ly α absorption, we infer $\log(N_{\text{H I}}/\text{cm}^{-2}) = 22.0 \pm 0.3$.

Appendix B.59: GRB 121209A ($z = 2.1$)

This data is published in Krühler et al. (2015), but is not used elsewhere. This short spectroscopic integration of 1.2ks reveals a very faint trace visible in the visual arm after binning. The spectrum is taken at high airmass and observations were discontinued due to the hardware limit of the telescope. No emission lines are detected in the spectrum. The redshift is adopted from Krühler et al. (2015).

Appendix B.60: GRB 121229A ($z = 2.707$)

These data formed the basis for GCN #14120⁶⁰, but is not published elsewhere. Taken under poor seeing conditions, a total of 4.8ks spectroscopic integration starting 2 hours after the *Swift* trigger yields a low S/N GRB afterglow continuum in all arms. Binning the spectrum reveals broad absorption troughs, which we identify as Ly β and Ly α at $z = 2.707$. Additionally, an intervening system at $z = 1.658$ is detected from absorption features of Mg II. From the absorption trough due to Ly α , we infer $\log(N_{\text{H I}}/\text{cm}^{-2}) = 21.7 \pm 0.2$. Due to strong contamination in the slit, the background is slightly over subtracted, cause the background to go negative in the center of the Ly α trough.

Appendix B.61: GRB 130131B ($z = 2.539$)

These data formed the basis for GCN #14286⁶¹ and is additionally published in Krühler et al. (2015). This is a late-time observation, taken long after the GRB afterglow has faded. In 7.2ks spectroscopic integration, emission lines identified as [O II] and [O III] are detected at a common $z = 2.539$, which we suggest is the redshift of the GRB.

Appendix B.62: GRB 130408A ($z = 3.758$)

The data presented here also formed the basis of GCN #14365⁶². The spectrum has not otherwise been published previously. The observations consists of two 600sec spectra taken 1.9hrs after the burst. We detect absorption features from a wide range of ions. We also detect intervening absorption at $z = 1.255$ and $z = 3.248$.

Appendix B.63: GRB 130418A ($z = 1.222$)

GCN #14390⁶³ is based on this spectrum, but it is not published elsewhere. Starting only 4.57 hours after the *Swift* trigger, 1.2ks observations contains a bright GRB afterglow continuum, visible across the entire spectral coverage of X-shooter. Superposed on the afterglow continuum are absorption features which we identify as C IV, Fe II, and Mg II, caused by an absorber at $z = 1.217$, and additional absorption from C IV at $z = 1.222$. The two systems are offset by $\sim 1500 \text{ km s}^{-1}$ and the proximity of the two

absorption systems in velocity space, suggests a possible association of the two systems with peculiar velocity affecting the measured redshift. We adopt $z = 1.222$ as the redshift of the GRB. Note, that this value is slightly different from the one reported in GCN # 14390.

Appendix B.64: GRB 130427A ($z = 0.340$)

This spectrum is also published in ? and Krühler et al. (2015) and additionally has formed the basis for GCN #14491⁶⁴. Starting 16.5 hours after the BAT trigger, these observations lasting $2 \times 600 \text{ s}$ contains a very bright GRB afterglow continuum across the total spectral coverage of X-shooter. In absorption we identify features from the following metal resonance lines: Fe II, Mn II, Mg II, Mg I, Ti II and additional line absorption from Ca II and Na I D. Simultaneously, we find emission lines from H α , H β , [O III], [O II]- all at common redshift of $z = 0.340$, which is the redshift of the GRB. This is one of the most energetic GRBs observed, and it's proximity along with the associated broad-lined Type Ic SN, 2013cq has caused it to be one of the more well studies GRBs.

Appendix B.65: GRB 130427B ($z = 2.780$)

This spectrum formed the basis of GCN #14493⁶⁵, but is not published otherwise. A short, $2 \times 600 \text{ s}$ spectroscopic integration obtained before twilight, 20.6 hours after the BAT trigger, captures a faint afterglow continuum visible across the entire spectral coverage at low S/N. Due to the low S/N, the metal lines are weak, but the broad absorption trough due to Ly α is detected. From this we measure the redshift to be $z = 2.780$ and provides a measure of the neutral hydrogen column density, $\log(N_{\text{H I}}/\text{cm}^{-2}) = 21.9 \pm 0.3$. The redshift is confirmed by the presence of Fe II at a consistent redshift.

Appendix B.66: GRB 130603B ($z = 0.356$)

This burst is the first sGRB observed with a potential associated kilonova(Tanvir et al. 2013; Berger et al. 2013). GCN #14757⁶⁶ was based on this spectrum, but it is not published elsewhere. Starting 8.2 hours after the *Swift* trigger, a total of 2.4 ks spectroscopic integration was obtained. Continuum is clearly detected across all arms from both host and afterglow and superposed are both absorption (Ca H & K and Mg II) and emission lines ([O II], H β , [O III], H α , and [S II]), all at a consistent redshift of $z = 0.356$, which is the redshift of the GRB.

Appendix B.67: GRB 130606A ($z = 5.913$)

The data presented here also formed the basis of GCN #14816⁶⁷ and is published in Hartoog et al. (2015). The observations consists of three $2 \times 600 \text{ s}$ visits starting 7.1 hrs after the burst at fairly high airmass. We detect absorption features from a wide range of ions at $z = 5.913$ as well as intervening absorption at $z = 2.3103, 2.5207, 3.4515, 4.4660, 4.5309, 4.5427, 4.6497$ and 4.7244 .

⁶⁰ <http://gcn.gsfc.nasa.gov/gcn3/14120.gcn3>

⁶¹ <http://gcn.gsfc.nasa.gov/gcn3/14286.gcn3>

⁶² <http://gcn.gsfc.nasa.gov/gcn3/14365.gcn3>

⁶³ <http://gcn.gsfc.nasa.gov/gcn3/14390.gcn3>

⁶⁴ <http://gcn.gsfc.nasa.gov/gcn3/14491.gcn3>

⁶⁵ <http://gcn.gsfc.nasa.gov/gcn3/14493.gcn3>

⁶⁶ <http://gcn.gsfc.nasa.gov/gcn3/14757.gcn3>

⁶⁷ <http://gcn.gsfc.nasa.gov/gcn3/14816.gcn3>

Appendix B.68: GRB 130612A ($z = 2.006$)

The spectral features of this spectrum has previously been reported in GCN #14882⁶⁸, but is not published elsewhere. Starting only 1.1 hour after the *Swift* trigger, 2×600 s spectroscopic integration captures a moderate S/N afterglow continuum across the total spectral coverage of X-shooter. At a consistent redshift of $z = 2.006$, absorption from the metal resonance lines Fe II, Mn II, Mg II, Mg I are identified. Additionally, Ly α is visible as a broad absorption trough, from we can infer $\log(N_{\text{H I}}/\text{cm}^{-2}) = 22.2 \pm 0.2$, which is in the upper end of the hydrogen column density distribution. The blue part of the GRB continuum exhibits a downturn in the continuum level which could indicate the presence of a significant amount of dust along the line-of-sight.

Appendix B.69: GRB 130615A ($z \sim 3$)

This spectrum has not previously been published. Starting only 45 minutes after the BAT trigger, 2×600 s spectroscopic integration carried on into the beginning twilight. Observed at very high airmass with a quickly varying background, a faint afterglow trace is visible across all arms of X-shooter, down to 4800 Å, confirming the approximate redshift suggested in GCN #14898⁶⁹.

Appendix B.70: GRB 130701A ($z = 1.155$)

These data formed the basis for GCN #14956⁷⁰ and is additionally published in Krühler et al. (2015). Starting 5.5 hours after the GRB trigger, 2×600 s reveals a bright continuum visible across the entire spectral coverage of X-shooter. Superposed are absorption features which we identify as due to Fe II, Mg II, Mg I, and Ca II - all at a consistent redshift of $z = 1.155$, which we take to be the redshift of the GRB.

Appendix B.71: GRB 130925A ($z = 0.347$)

This spectrum has already been used in GCN #15250⁷¹ and is additionally published in Schady et al. (2015) and Krühler et al. (2015). Observations of this burst began with X-shooter 3.5 hours after the *Swift* trigger. 6 ks spectroscopic integration captures a heavily dust obscured afterglow ($A_V = 5.9 \pm 0.7(?)$), with the spectrum primarily dominated by host emission lines. All the nebular lines ([O II], H γ , H β , [O III], H α , [N II], [S II]) are well detected at $z = 0.347$, which we as the redshift of the GRB. This spectrum is taken under ESO programme ID: 091.A-0877(A) (PI: Schady).

Appendix B.72: GRB 131011A ($z = 1.874$)

This data formed the basis for #15330⁷², but is not published elsewhere. Starting ~ 1.5 days after the Fermi-GBM trigger, 4.5 ks spectroscopic integration captures a modest S/N GRB afterglow continuum all the way down to ~ 3200 Å. Imprinted on the continuum are absorption features, which we identify as due to Ly α , Fe II, Mg II, Mg I at the same redshift, which we measure to be $z = 1.874$. From the broad absorption trough due to Ly α , we

infer $\log(N_{\text{H I}}/\text{cm}^{-2}) = 22.0 \pm 0.3$. This spectrum is taken under ESO programme ID: 092.D-0056(A) (PI: Rau).

Appendix B.73: (CHECK ME - Bright un-used spectrum) GRB 131030A ($z = 1.296$)

This data has not been published before. Starting 3.4 hours after the *Swift* trigger, 6×600 s exposure taken under good conditions, contains a bright GRB afterglow continuum across the entire spectral coverage of X-shooter. A myriad of absorption features are superposed on the afterglow continuum which we identify as being caused by Si IV, Si II, C IV, Al II, Al III, Zn II, Cr II, [Ni II], Fe II, [Ni II]*, and Fe II* at $z = 1.296$. A very strong Mg II-absorber is also detected, intervening the line-of-sight at $z = 1.164$ with lines from Si II, C IV, Al III, Al II, Fe II, Mn II, and many more.

Appendix B.74: GRB 131103A ($z = 0.599$)

This spectrum has already been used to form the basis for GCN #15451⁷³ and is additionally published in Krühler et al. (2015). Starting 5.8 hours after the BAT trigger, 4×600 s exposure captures a modest S/N continuum across all arms. Imprinted on the continuum are absorption features identified as due to Fe II and Mg II as well as emission lines from [O II], H δ , H γ , H β , [O III], H α , and [N II]. All the lines are measured at a consistent redshift of $z = 0.599$, which we take as the redshift of the GRB.

Appendix B.75: GRB 131105A ($z = 1.686$)

This spectrum has already been used in shaping GCN #15450⁷⁴ and is additionally published in Krühler et al. (2015). Starting only 1.3 hours after the *Swift* trigger, a total of 4.8 ks spectroscopic integration contains a low S/N GRB afterglow continuum across the entire spectral coverage of X-shooter. There are deviations from the continuum at both emission and absorption. We identify lines from H β , [O III], and H α in emission and Fe II, and Mg II in absorption. All lines are at a consistent $z = 1.686$, which is probably the redshift of the GRB. Absorption lines at shorter wavelengths are also detected, but at low significance due to an apparent downturn in the continuum caused by the presence of dust local to the burst.

Appendix B.76: GRB 131117A ($z = 4.042$)

This spectrum has previously been used in GCN #15494⁷⁵, but is not published in a refereed paper. Starting only 68 minutes after the BAT trigger, 4.8 ks spectroscopic integration secures afterglow continuum for this bursts, which is measured to be at $z = 4.042$. A moderate S/N GRB afterglow continuum is detected down to ~ 6100 Å, signifying the onset of the Ly α forest, with part of the forest also visible. Metal absorption lines from Si II and Si IV are detected at a consistent redshift.

Appendix B.77: GRB 131231A ($z = 0.642$)

This spectrum has previously been published in Krühler et al. (2015) and additionally forms the basis for GCN #15645⁷⁶. This

⁶⁸ <http://gcn.gsfc.nasa.gov/gcn3/14882.gcn3>

⁶⁹ <http://gcn.gsfc.nasa.gov/gcn3/14898.gcn3>

⁷⁰ <http://gcn.gsfc.nasa.gov/gcn3/14956.gcn3>

⁷¹ <http://gcn.gsfc.nasa.gov/gcn3/15250.gcn3>

⁷² <http://gcn.gsfc.nasa.gov/gcn3/15330.gcn3>

⁷³ <http://gcn.gsfc.nasa.gov/gcn3/15451.gcn3>

⁷⁴ <http://gcn.gsfc.nasa.gov/gcn3/15450.gcn3>

⁷⁵ <http://gcn.gsfc.nasa.gov/gcn3/15494.gcn3>

⁷⁶ <http://gcn.gsfc.nasa.gov/gcn3/15645.gcn3>

spectrum, observed the following year (20.2 hours after the *Swift* trigger), consists of 4×600 s exposures. A high S/N GRB afterglow continuum is detected all the way though the X-shooter arms. We identify absorption features imprinted in the continuum as caused by Fe II, Mg II, and Ca H & K at a consistent $z = 0.642$. By subtracting off the bright afterglow continuum, we readily detect emission lines arising from [O II], H γ , H β , [O III], and H α in the GRB host galaxy.

Appendix B.78: GRB 140114A ($z = \sim 2.8?$)

Appendix B.79: GRB 140213A ($z = 1.208$)

Appendix B.80: GRB 140301A ($z = 1.416$)

Appendix B.81: GRB 140311A ($z = 4.95$)

Appendix B.82: GRB 140430A ($z = 1.601$)

Appendix B.83: GRB 140506A ($z = 0.889$)

The data presented here has formed the basis of GCN # 16214⁷⁷ and is published in Fynbo et al. (2014) and Heintz et al. (2017b). The observations consists of 4×600 sec at 8.8 and 33 hours after the burst. We detect absorption features from a wide range of ions, together with molecular absorption from CH⁺, all at $z = 0.889$. The optical/near-infrared afterglow reveal an unusual steep extinction curve which is found to be caused by dust immediate to the burst.

Appendix B.84: GRB 140515A ($z = \sim 6.32?$)

Appendix B.85: GRB 140614A ($z = 4.233$)

Appendix B.86: GRB 140622A ($z = 0.959$)

Appendix B.87: GRB 141028A ($z = 2.332$)

Appendix B.88: GRB 141031A ($z = na$)

Appendix B.89: GRB 141109A ($z = 2.993$)

Appendix B.90: GRB 150206A ($z = 2.087$)

Appendix B.91: GRB 150301B ($z = 1.517$)

Appendix B.92: GRB 150403A ($z = 2.06$)

Appendix B.93: GRB 150423A ($z = 1.394$)

Appendix B.94: GRB 150428A ($z = na$)

Appendix B.95: GRB 150514A ($z = 0.807$)

Appendix B.96: GRB 150518A ($z = 0.256$)

Appendix B.97: GRB 150616A ($z = 1.188$)

Appendix B.98: GRB 150727A ($z = 0.313$)

Appendix B.99: GRB 150821A ($z = 0.755$)

Appendix B.100: GRB 150831A ($z = na$)

Appendix B.101: GRB 150910A ($z = 1.359$)

Appendix B.102: GRB 150915A ($z = 1.968$)

Appendix B.103: GRB 151021A ($z = 2.330$)

The data presented here also formed the basis of GCN # 18426⁷⁸ and is not published elsewhere. The observation was carried out in RRM starting 44 minutes after the GRB trigger. We detect absorption features from a wide range of ions at $z = 2.330$ as well as intervening absorption at $z = 1.49$.

Appendix B.104: GRB 151027B ($z = 4.063$)

Appendix B.105: GRB 151029A ($z = 1.423$)

Appendix B.106: GRB 151031A ($z = 1.167$)

Appendix B.107: GRB 160117B ($z = 0.87$)

Appendix B.108: GRB 160203A ($z = 3.517$)

The data presented here also formed the basis of GCN # 18982⁷⁹ and is not published elsewhere. The observation was carried out in RRM starting 18 minutes after the GRB trigger. We detect absorption features from a wide range of ions at $z = 3.517$ as well as intervening absorption at $z = 2.203$.

⁷⁷ <http://gcn.gsfc.nasa.gov/other/140506A.gcn3>

⁷⁸ <http://gcn.gsfc.nasa.gov/gcn3/18982.gcn3>

⁷⁹ <http://gcn.gsfc.nasa.gov/gcn3/18982.gcn3>

Appendix B.109: GRB 160228A ($z = 1.64$)

Appendix B.110: GRB 160303A ($z = na$)

Appendix B.111: GRB 160314A ($z = 0.726$)

Appendix B.112: GRB 160410A ($z = 1.717$)

Appendix B.113: GRB 160425A ($z = 0.555$)

Appendix B.114: GRB 160625B ($z = 1.406$)

Appendix B.115: GRB 160804A ($z = 0.736$)

The data presented here also formed the basis of GCN # 19773⁸⁰, and is published in Heintz et al. (2017a). Observations started 22.37 hours after the BAT trigger and lasted for 2.4ks. The afterglow continuum is detected across the entire spectral coverage of X-shooter and absorption lines from Mg I, Mg II, Fe II and Al II are found at $z = 0.736$. At the same redshift, emission lines from [O II], [O III], H α , H β , H γ , [N II], [S II], [S III] are found. A second epoch, lasting 3.6ks, is obtained after the afterglow has faded, confirming the emission line detections. The host galaxy is found to have a roughly solar metallicity and is among the most luminous GRB hosts at $z < 1$.

Appendix B.116: GRB 161001A ($z = 0.891?$)

Appendix B.117: GRB 161007A ($z = 4.6$??? NEW!!!)

This data has not been published elsewhere. Observations for GRB 161007A started 323 hours after the burst trigger and contains the potential host. 4 x 600 seconds of observations reveals a faint continuum rising abruptly above the noise at ~ 685 nm and continuing through 2100 nm. A very low significance continuum is detected at shorter wavelengths, down to ~ 600 nm. If the host is located at $z \sim 4.6$, the drop in continuum flux is the Lyman alpha break and the absence of nebular emission lines is due to [O II] being shifted out of the wavelength coverage. Alternatively, an early-type host at $z = 0.71$ could exhibit the 400 nm break at 600 nm, but due to the preference of long-duration GRBs for star-forming galaxies, this is the least likely explanation, why we believe the high- z solution.

Appendix B.118: GRB 161014A ($z = 2.823$)

The data presented here also formed the basis of GCN # 20061⁸¹, but is not published elsewhere. Starting 11.6 hours after the GRB trigger, 4.8 ks of integration time captures the afterglow continuum across all three spectroscopic arms. A broad absorption trough due to Lyman alpha is visible, along with metal absorption features from Mg II, Si II, C II, C IV, Al II, Al III, and Fe II, all at $z = 2.823$. Similar to GRB 140506 (Fynbo et al. 2014), a break in the continuum shape is detected bluewards of 600 nm, possibly signifying some anomalous form of extinction.

Appendix B.119: GRB 161023A ($z = 2.710$)

Appendix B.120: GRB 161117A ($z = 1.549$)

⁸⁰ <http://gcn.gsfc.nasa.gov/gcn3/19773.gcn3>

⁸¹ <http://gcn.gsfc.nasa.gov/gcn3/20061.gcn3>